A High-Resolution Modeling Study of the 24 May 2002 Dryline Case during IHOP. Part I: Numerical Simulation and General Evolution of the Dryline and Convection

MING XUE

School of Meteorology, and Center for Analysis and Prediction of Storms, University of Oklahoma, Norman, Oklahoma

WILLIAM J. MARTIN

Center for Analysis and Prediction of Storms, University of Oklahoma, Norman, Oklahoma

(Manuscript received 8 November 2004, in final form 21 June 2005)

ABSTRACT

Results from a high-resolution numerical simulation of the 24 May 2002 dryline convective initiation (CI) case are presented. The simulation uses a 400 km $\times$ 700 km domain with a 1-km horizontal resolution grid nested inside a 3-km domain and starts from an assimilated initial condition at 1800 UTC. Routine as well as special upper-air and surface observations collected during the International H_2O Project (IHOP_2002) are assimilated into the initial condition. The initiation of convective storms at around 2015 UTC along a section of the dryline south of the Texas panhandle is correctly predicted, as is the noninitiation of convection at a cold-front–dryline intersection (triple point) located farther north. The timing and location of predicted CI are accurate to within 20 min and 25 km, respectively. The general evolution of the predicted convective line up to 6 h of model time also verifies well.

Mesoscale convergence associated with the confluent flow around the dryline is shown to produce an upward moisture bulge, while surface heating and boundary layer mixing are responsible for the general deepening of the boundary layer. These processes produce favorable conditions for convection but the actual triggering of deep moist convection at specific locations along the dryline depends on localized forcing. Interaction of the primary dryline convergence boundary with horizontal convective rolls on its west side provides such localized forcing, while convective eddies on the immediate east side are suppressed by a downward mesoscale dryline circulation. A companion paper analyzes in detail the exact processes of convective initiation along this dryline.

1. Introduction

The dryline, defined as the narrow zone of strong horizontal moisture gradient at and near the surface, is frequently observed in the western Great Plains of the United States. In this region, the line is usually a boundary between warm, moist air from the Gulf of Mexico and hot, dry continental air from the semiarid southwestern states or the Mexican plateau. The dryline is often the focus of convection initiation (CI). Rhea (1966) found that convection developed within 200 n mi of the dryline 70% of the time. Surface wind convergence commonly associated with drylines is believed to be an important reason for frequent CI along the line. Another reason is that the dryline represents the westmost boundary of the moist air from the Gulf, and it is where conditions first become favorable for upper-level disturbances propagating out of the Rockies to trigger convection. In spite of a number of existing studies (e.g., Bluestein and Parker 1993; Ziegler and Hane 1993; Ziegler et al. 1995; Shaw et al. 1997; Atkins et al. 1998; Ziegler and Rasmussen 1998; Hane et al. 2002; Peckham et al. 2004), the exact processes by which convection is initiated are still not well understood (Hane et al. 1993). The exact timing and location that convection is initiated along drylines are even harder to predict.

During the 2002 International H_2O Project (IHOP_2002; Weckwerth et al. 2004), a dryline formed on 24 May and intense convection was initiated along the line in the afternoon. The event was intensively

Corresponding author address: Dr. Ming Xue, School of Meteorology, University of Oklahoma, 100 E. Boyd, Norman, OK 73019.
E-mail: mxue@ou.edu

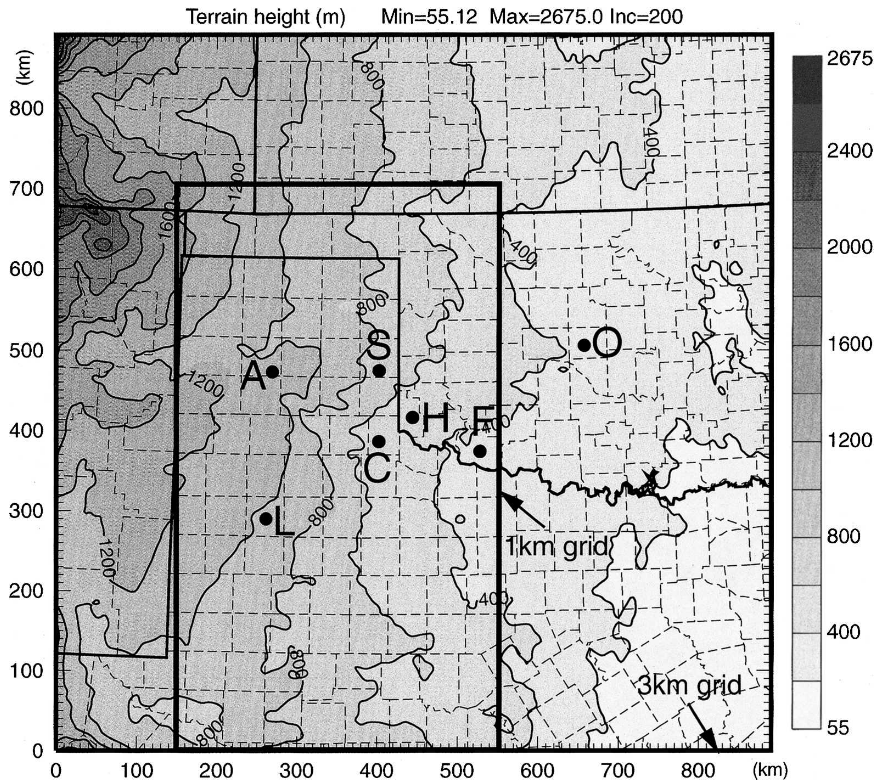

FIG. 1. The 3-km model domain with shaded terrain-elevation contours. The nested 1-km domain is indicated by the rectangular box, which used a separate higher-resolution terrain definition. The 1-km grid shares the south boundary with the 3-km one. Letters A, L, S, C, H, F, and O in the figure indicate the locations of Amarillo, Lubbock, Shamrock, and Childress in Texas, and Hollis, Frederick, and Oklahoma City in Oklahoma, respectively. Also shown are county and state boundaries.

observed during the field experiment for the purpose of studying CI and the possible interaction of the dryline with an intersecting cold front (see a highlight of the case in Weckwerth et al. 2004). A rich set of special observations was collected during the field experiment and additional data were gathered from various networks of surface stations [see Weckwerth et al. (2004) for lists and maps of IHOP specific instruments and their deployment during IHOP_2002]. The special observational platforms include several research aircrafts with airborne Doppler radars, lidars, dropsondes and other instruments, the S-band dual-polarization Doppler radar (S-Pol), two Doppler-on-Wheels (DOW), Shared Mobile Atmospheric Research and Teaching Radar (SMART-R), and mobile X-band polarimetric radar (X-Pol) radars, mobile surface and upper-air sounding systems, and Mobile Integrated Profiling System (MIPS). In addition, the primary regions of CI fall within the range of several Weather Surveillance Radar-1988 Doppler units (WSR-88Ds), in particular, those of Amarillo (KAMA) and Lubbock (KLBB), Texas, and Frederick (KFDR), Oklahoma (see Fig. 1 for a map of the vicinity). At the surface, the Oklahoma Mesonet and West Texas Mesonet provide additional observations near and around the CI regions along the dryline. The detailed observational data provide us with an unprecedented opportunity to study the CI processes from both observational and modeling perspectives. In fact, there are currently several studies on this case, each with a somewhat different focus (e.g., Geerts et al. 2006; Holt et al. 2006; Wakimoto et al. 2006).

In this study, a nonhydrostatic mesoscale model is used to simulate the evolution of the dryline and the intersecting cold front as well as the initiation and development of convective storms along and near the dryline and cold front. A nested 700 km $\times$ 400 km model domain at 1-km horizontal resolution is used, which is large enough to cover the entire dryline and the portion of the cold front within the region of interest, and the horizontal resolution is sufficient for resolving organized boundary layer (BL) eddies and convective rolls, and for the explicit simulation of the ini-

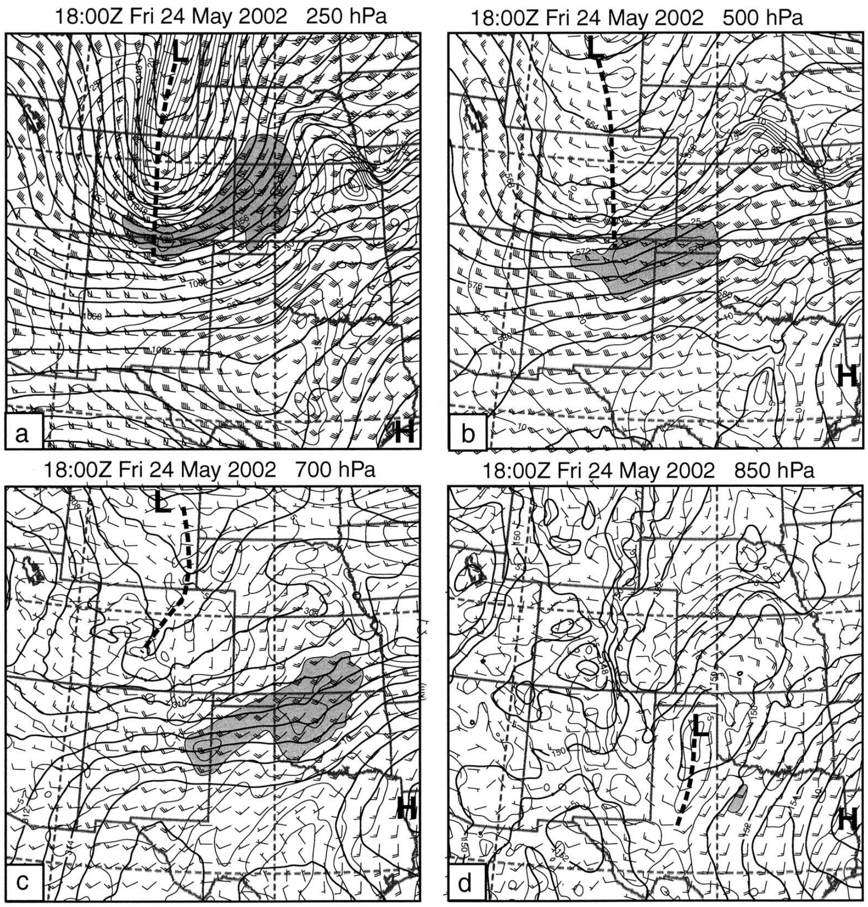

FIG. 2. Geopotential height (thick black contours, 10 m), wind speed (thin black contours, m s^{-1}), and wind barbs (one full barb = 5 m s^{-1}) at 1800 UTC 24 May 2002, at (a) 250-, (b) 500-, (c) 700-, and (d) 850-hPa levels. Bold dashed lines indicate the locations of trough lines, and areas with wind speed exceeding 35 m s^{-1} at 250 hPa, 25 m s^{-1} at 500 hPa, 12.5 m s^{-1} at 700 hPa, and 10 m s^{-1} at 850 hPa are shaded gray.

tiation and development of moist convection. Existing modeling studies, most notably Ziegler et al. (1997) and Peckham et al. (2004), have either used a nested high-resolution (1 km) domain that might have been too small to permit realistic development of regular-aspect-ratio horizontal convective rolls (HCRs) or employed idealized terrain and initial and boundary conditions, which limit the realism of results and one's ability to compare directly with real observations.

In the rest of this paper, we first introduce the case in section 2. The initial condition and setup of the numerical experiments are described in section 3. In section 4, model-predicted moist convection is verified against radar observations, and the structure and evolution of the boundary layer (BL) and the dryline, as well as the effect of the BL evolution on convective initiation, are discussed. The development of BL convective eddies and horizontal rolls and their structure and effect on CI are also discussed. A summary is given in section 5. In the second part of this paper (Xue and Martin 2006, hereafter Part II) the exact CI processes are analyzed in detail and a conceptual model for dryline CI that involves HCR–dryline interaction is proposed.

2. The 24 May 2002 dryline case

At 1800 UTC (hereafter all times are UTC) 24 May 2002, a deep trough was situated over eastern Wyoming and central Colorado on the 250-hPa chart (Fig. 2a). Associated with this trough was a jet maximum located over northwestern Kansas with winds over 35 m s^{-1}. The Texas panhandle, where convection was initiated a little over 2 h later, was located in the right-rear quadrant of the 250-hPa jet streak, a location favorable for convection due to jet-induced ageostrophic circulation. The winds over the Texas panhandle were west-southwesterly at this level, but turned southwesterly as the flow crossed the western Oklahoma and Texas border. This wind shift line extended south into south-central Texas, and a wind minimum is found associated with this trough. At this and all other levels (Fig. 2), a high was located east of Texas over Louisiana, which at the low levels brought warm moist air into central Texas and Oklahoma from the Gulf of Mexico. At the 500-hPa level, a deep trough was also located over Wyoming and Colorado (Fig. 2b), and the Texas panhandle was located at the bottom of this trough, in a broad, more or less straight, and relatively strong west-southwesterly flow. At the 700-hPa level (Fig. 2c), a strong west-southwesterly flow was over the Texas panhandle and between the high to its southeast and a trough to its northwest. At the 850-hPa level (Fig. 2d), a closed circulation center is found in the eastern Texas panhandle, which is also seen at the surface (Fig. 3a) and corresponds roughly to the intersecting point of the surface cold front and dryline, or the "triple point" (Fig. 3a). Extending from the circulation center southward at 850 hPa is a line with strong horizontal wind shear, which is actually the location of the dryline. This line separates the mostly westerly flow to its west and the mostly southerly flow to its east. The latter exceeds 10 m s^{-1} farther east in west-central Texas, bringing moist air from the Gulf into the region east of the dryline (Fig. 2d). The surface flow pattern over the central plains is similar to that at 850 hPa (Figs. 3a and 2d). Behind the cold front in the Texas panhandle is a pool of rather shallow cold air that pushed the cold front southeastward, toward the dryline (Fig. 3a). As the cold front advanced, the triple point shifted southward, and the cold front and dryline behaved like a "closing zipper," as described by Wakimoto et al. (2006). On the east side of the triple point, the front was actually pushed northward in the next few hours. By 2000, it was located close to the Oklahoma panhandle (not shown). At 1200, the local morning and the initial time of our 3-km preforecast cycle, the dryline was located at the Texas–New Mexico border, and the surface closed vortex was located in the western Texas panhandle. This vortex migrated eastward along the cold front to its position at 1800 and continued on northeastward. The latter was also observed by Doppler radar (Wakimoto et al. 2006).

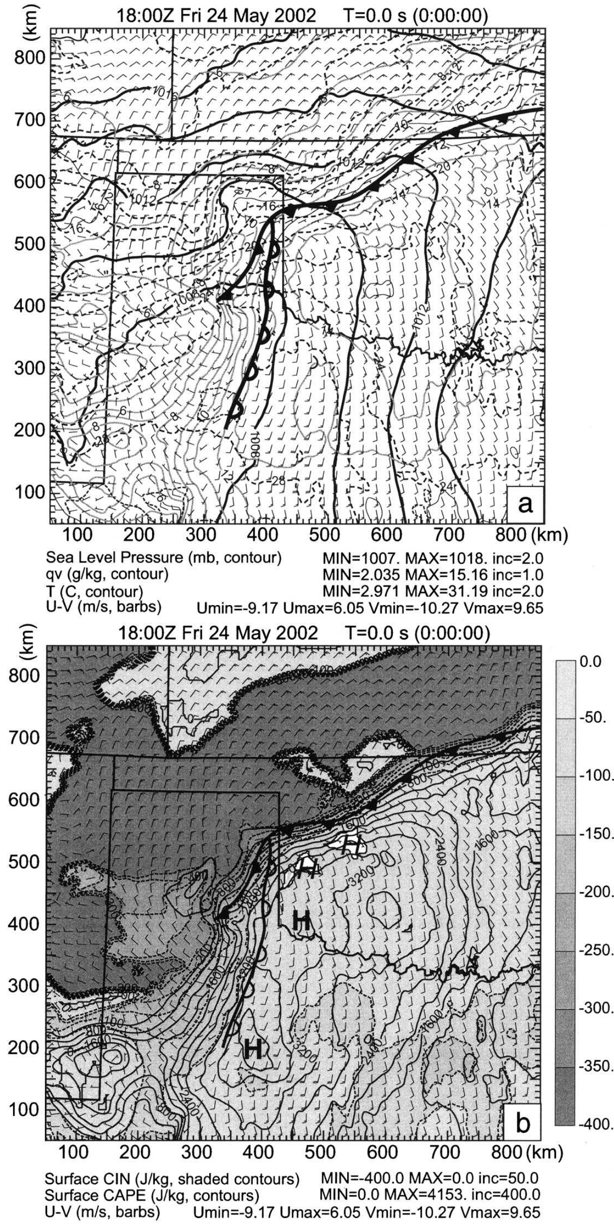

FIG. 3. The surface fields plotted from ADAS analysis at 1800 UTC 24 May 2002: (a) Mean sea level pressure (thick black contours, hPa), temperature (thin dashed contours, °C), water vapor mixing ratio (thin gray contours, g kg^{-1}), and the wind field (full barb represents 5 m s^{-1}, half barb 2.5 m s^{-1}); (b) wind fields, CAPE (thick contours, J kg^{-1}, with maximum centers marked by **H**), and CIN (dashed contours with gray shading, J kg^{-1}, values less than -400 J kg^{-1} are shown with the same dark gray, with maximum value centers marked by ***H***). Regions with zero CIN are not shaded. Cold front and dryline are marked by standard symbols.

Figure 3b shows the convective available potential energy (CAPE) and convective inhibition (CIN) maps at 1800. A region of over 3200 J kg^{-1} of CAPE is seen extending from SW Oklahoma south-southwestward into western-central Texas, parallel to and bordering the dryline on the west side. A local CAPE maximum of over 3600 J kg^{-1} (denoted by H) is found at the SW corner of Oklahoma, while another, larger maximum of over 4000 J kg^{-1} is found farther south. The latter maximum is believed to be unrealistic however and is responsible for model CI that is too early in that region. In addition, patches of zero CIN are seen in Fig. 3b (centers marked by H) and are close to the cold front. In general, absolute CIN east of the dryline was less than 50 J kg^{-1}. Not surprisingly, convective cells, as will be discussed next, were initiated a little over 2 h later in between the CAPE maximum at SW Oklahoma and the 1800 dryline located to the west.

Figure 4 shows the Geostationary Operational Environmental Satellite (GOES) visible images taken at 1900, 2000, and 2045 on 24 May 2002. At all three times, a broad region north of the surface cold front is covered by mostly stratiform clouds. At 1900, western Texas and the Texas panhandle south of the cold front are generally free of cloud cover, except for some small shallow clouds (as indicated by white arrows in Fig. 4a) extending southwestward from SW Oklahoma, which are believed to be related to BL eddy and roll activities. The general clearance from cloud cover leads to strong heating at the surface.

By 2000, one identifiable large cumulus cloud is seen developing near Childress, Texas (see map in Fig. 1 and white arrow in Fig. 4b). This cloud is also seen in the radar observations (Fig. 8e) at this time though the radar echo is still weak. Smaller clouds are also seen farther SW of this cumulus, and they generally form along the dryline. By 2045 (Fig. 4c), anvils from several fully developed cumulus clouds are now seen and the initial cell that started before 2000 has moved right over the SW corner of Oklahoma (see arrows in Fig. 4c). The radar reflectivity field at this time reveals several individual cells embedded within this convective line (Fig. 8h). It is clear that the initiation of convection started close to 2000 and several cells became fully developed by 2045.

During the field experiment, a decision was made in the morning to focus the field operations on the cold-front–dryline triple point, expected to be located near Shamrock, Texas, in the afternoon (see map in Fig. 1). Extensive and very detailed observations were collected on the triple point and the intersecting dryline and cold front (Weckwerth et al. 2004; Geerts et al. 2006), and some of the analyses are found in Wakimoto et al. (2006). However, initiation of convection did not occur at the triple point, but at about 100 km to the south along the dryline. The exact reason for this non-initiation is certainly worth investigating but is not the focus of this paper. In the next section, we discuss the numerical simulation of this case, with a focus on the dryline CI to the south.

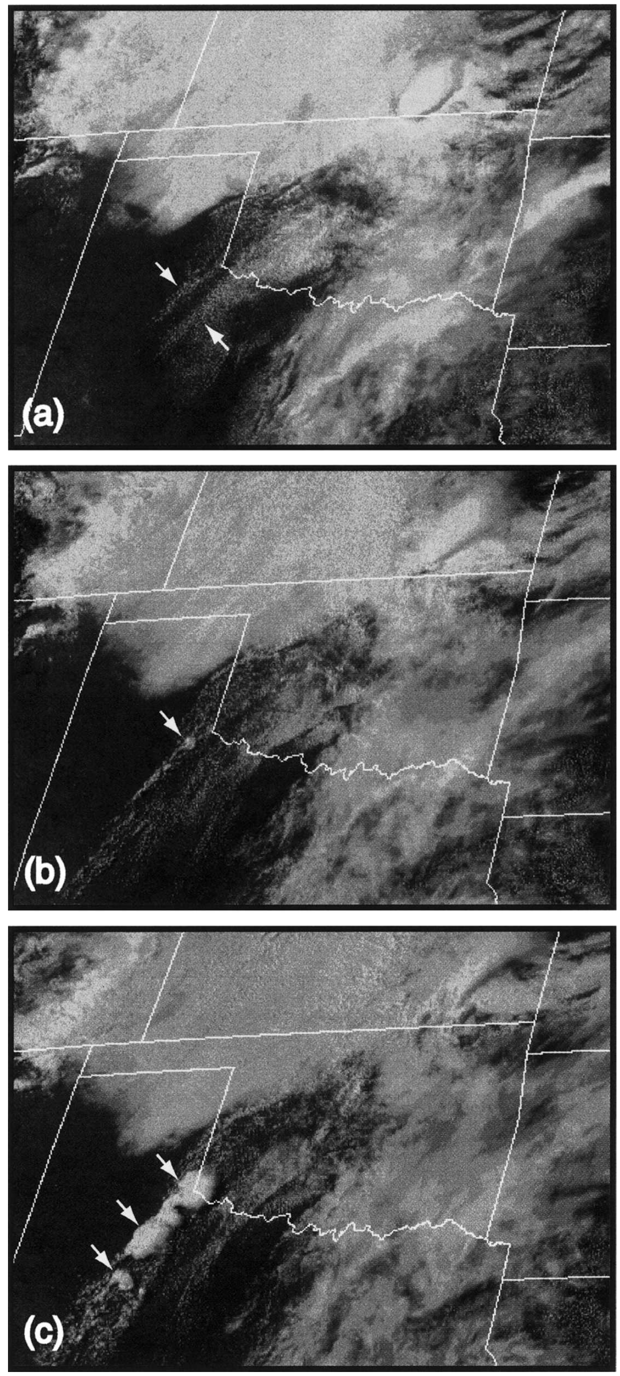

FIG. 4. GOES visible satellite images taken at (a) 1900, (b) 2000, and (c) 2045 UTC 24 May 2002.

3. Setup of numerical simulations and model initial conditions

The numerical model used in this study is the Advanced Regional Prediction System (ARPS; Xue et al. 2000, 2001, 2003), a general-purpose nonhydrostatic model suitable for mesoscale and convective-scale simulation and prediction. The data analysis component of the model system, the ARPS Data Analysis System (ADAS; Brewster 1996), is used to generate the initial and boundary conditions for the model simulations. The basic analysis scheme used by ADAS is the Bratseth (1986) successive correction method, which in theory converges to the optimal interpolation scheme through multiple iterations. In the ADAS analyses, multiple analysis passes were performed, with each pass including observations of different scales and also using different spatial influence radii. Specifically, two one-way nested grids were used, one at 3-km and one at 1-km horizontal resolution (Fig. 1). The vertical resolution changes from 20 m near the ground to about 800 m at the model top located at about 20 km above mean sea level (MSL) and the vertical grid stretching uses a cubic function as described in Xue et al. (1995). Fifty vertical layers were used, with about 12 layers located below 2 km above ground level (AGL).

The terrain elevations on the 3- and 1-km grids were derived from the U.S. Geological Survey (USGS) 30-s terrain-elevation dataset, by direct interpolation plus two passes of nine-point smoothing. The 1-km terrain was blended with the 3-km one near the 1-km grid boundary to ensure terrain continuity at the nesting boundary. The soil and vegetation types, leaf-area index, surface roughness, and albedo were derived from datasets of 1-km resolution. Furthermore, three types of soil were allowed within each grid cell, with each type carrying a percentage weight determined by the data [see Xue et al. (2003) for details on the ARPS soil–vegetation dataset].

Intermittent data assimilations were performed between 1200 and 1800. A 6-h ARPS forecast starting from the ADAS analysis at 1200 was first performed; another analysis was then performed at 1800 using the 6-h forecast as the background. This new analysis then served as the initial condition (IC) for the ensuing forecast. Lateral boundary conditions (BCs) for the 3-km grid were provided by ADAS 3-hourly analyses, using as the background the 6-hourly National Centers for Environmental Prediction (NCEP) Eta analyses and the 3-h forecasts at intermediate times. The ADAS analyses incorporated all available upper-air soundings and many surface observations within the model domain. The latter include those from Automated Surface Observing System (ASOS) stations, the Oklahoma Mesonet, the Southwest Kansas Mesonet, the South-central Kansas Mesonet, and the Atmospheric Radiation Measurement (ARM) Program Surface Meteorological Observation System (SMOS) network. Together, there are about 245 surface stations within the 3-km domain, providing a rather complete high-density data coverage for the near-surface atmospheric conditions. Within the 3-km domain, there are five National Weather Service (NWS) radiosonde sites plus four ARM upper-air sounding sites located in Oklahoma. At 1200, and 1800, there were five NWS soundings and one ARM sounding available. Additional details on the individual networks and the station distributions can be found in Stano (2003). Figure 5 shows the surface (10 m) water vapor mixing ratio and wind vectors overlaid with the surface observations used in the analysis/initial condition at 1800.

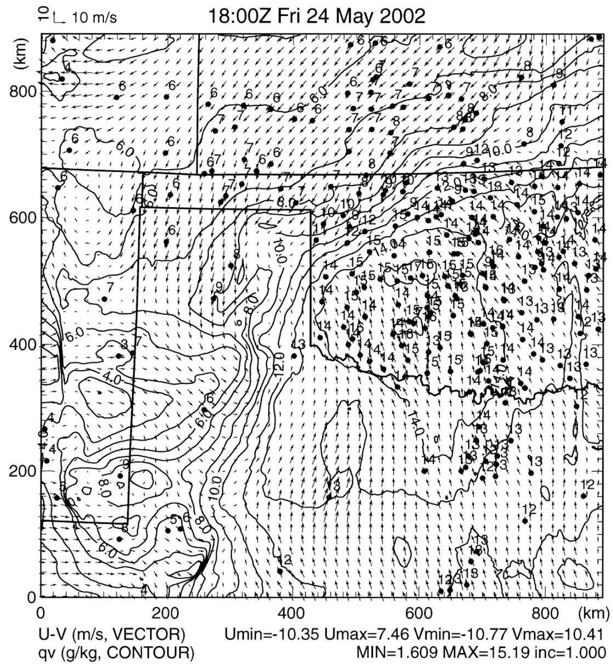

FIG. 5. Plot of surface winds (every sixth grid point) and q_v (g kg^{-1}) field at the initial condition time, 1800 UTC, with surface station observations of q_v overlaid.

The ADAS analyses used four passes. Rawindsondes were used in the first two passes with large effective radii of influence, while the denser surface networks were used in the second through fourth passes, with smaller effective radii of influence. Tables 1 and 2 detail the horizontal and vertical effective radii of influence used in each pass and for each variable.

After the 6-h preforecast assimilation period that started at 1200, the 3-km ARPS was run from 1800 for 6 h. This 3-km run provided boundary conditions for the nested 1-km grid at 5-min intervals. The initial con-

TABLE 1. Values of radii of influence used in ADAS vs pass number.

Pass number	Horizontal (km)	Vertical (m)
1	300	800
2	120	400
3	80	300
4	60	200

TABLE 2. Range scale factors for specific variables used in ADAS. Radius of influence for a specific variable is the value from Table 1 times a variable-specific scale factor given in this table.

Variable	Scale factor
U	0.9
V	0.9
Pressure	1.0
Potential temperature	1.0
Humidity	0.9

ditions of the 1-km grid were directly interpolated from the 3-km analysis at 1800. Compared with an earlier simulation that did not include a 6-h 3-km preforecast cycle, the dryline structure is better developed at and near the time of CI. The CI in the earlier 1-km simulation that "cold started" at 1800 was delayed by nearly 2 h. The CI in the 3-km simulation, even with assimilation cycling, is also late by over 1 h.

The ARPS model was used with its complete suite of physics except for cumulus parameterization. The advection scheme was fourth order in the horizontal and second order in the vertical. The physics packages used by both grids include Lin et al. (1983) 3-ice microphysics, 1.5-order turbulent kinetic energy (TKE)–based subgrid-scale turbulence parameterization, an improved version of Noilhan and Planton (1989)–type two-layer soil–vegetation model (Ren and Xue 2004; Xue and Ren 2004), TKE-based PBL-mixing parameterization (Sun and Chang 1986; Xue et al. 1996), and the National Aeronautics and Space Administration (NASA) Goddard Space Flight Center (GSFC) long- and shortwave radiation package (Chou 1990, 1992; Chou and Suarez 1994).

Lacking measurements of soil temperature and moisture, the soil model was initialized at 1200 using the fields in the operational analysis for the Eta Model, and the ARPS 6-h forecast of soil conditions is carried into the 1800 simulations without further modification. Previous idealized experiments (e.g., Shaw 1995; Ziegler et al. 1995; Grasso 2000) have shown sensitivity of dryline structure and evolution to soil moisture conditions, and Holt et al. (2006) studied specifically the effect of land–atmosphere interactions on the current case. They found subtle yet significant impact of the quality (e.g., resolution) of the soil moisture and temperature information on CI, in their experiments with 12-h assimilation cycles that started at 0000 on 24 May 2002 using nested grids at 12- and 4-km resolutions. They found the Eta soil conditions were drier in the Texas panhandle region than those derived from the High-Resolution Land Data Assimilation System (HRLDAS; Chen et al. 2004), leading to deeper convective boundary layer than the HRLADS case. In our current simulation, the good timing and location of the initiation of convection along the dryline south of the Texas panhandle suggest that the prediction of the land surface conditions are reasonable. In the future, more frequent assimilation cycles will be tested within the 6-h preforecast period, which hopefully will further improve the soil condition and boundary layer structure at 1800.

For the 1-km run, gridded output at 1-min intervals were saved and analyzed with the help of various animations. In this paper, only results from the 1-km grid will be presented.

4. Results

a. *The forecast of convective storms, boundary layer eddies, and their general evolution*

In Fig. 6, we compare the model-predicted composite reflectivity, Z, at 2100, 2200, and 2300 on 24 May, and at 0000 on 25 May 2002, against the corresponding radar observations. Here composite reflectivity is defined as the maximum reflectivity in the vertical column, and the model reflectivity is derived from predicted hydrometeors, including rainwater, snow, and hail mixing ratios. The actual formula used can be found in Tong and Xue (2005). At 2000, no significant reflectivity existed in either the model or radar observations. The first echo exceeding 20 dBZ that occurred along the dryline near Childress, Texas (cf. Fig. 4 and Figs. 8e–h) occurred between 2005 and 2015 in both the model and in radar observations. This stage of convective initiation will be discussed more later.

At 2100, the radar observations exhibit convection extending from the southwest corner of Oklahoma south-southwestward, into about four counties (Fig. 6e). The most intense storms were at the northern end of this convective line and these storms also initiated earliest. In the model, similarly located storms are seen at this time, although the line of convection is about half as long. These storms were initiated along and close to the moist side of the dryline moisture gradient zone, and the surface flow shows strong convergence into the dryline region (Fig. 6a).

In the model, more scattered convection was also initiated in northwestern Oklahoma, along the slow-moving surface cold front where surface convergence is strong (Fig. 6a). These convective cells were not observed by radar in this exact region, perhaps because the real-world condition was less conducive to convection in this region. Scattered storm cells were observed farther northeast, in north-central Oklahoma and

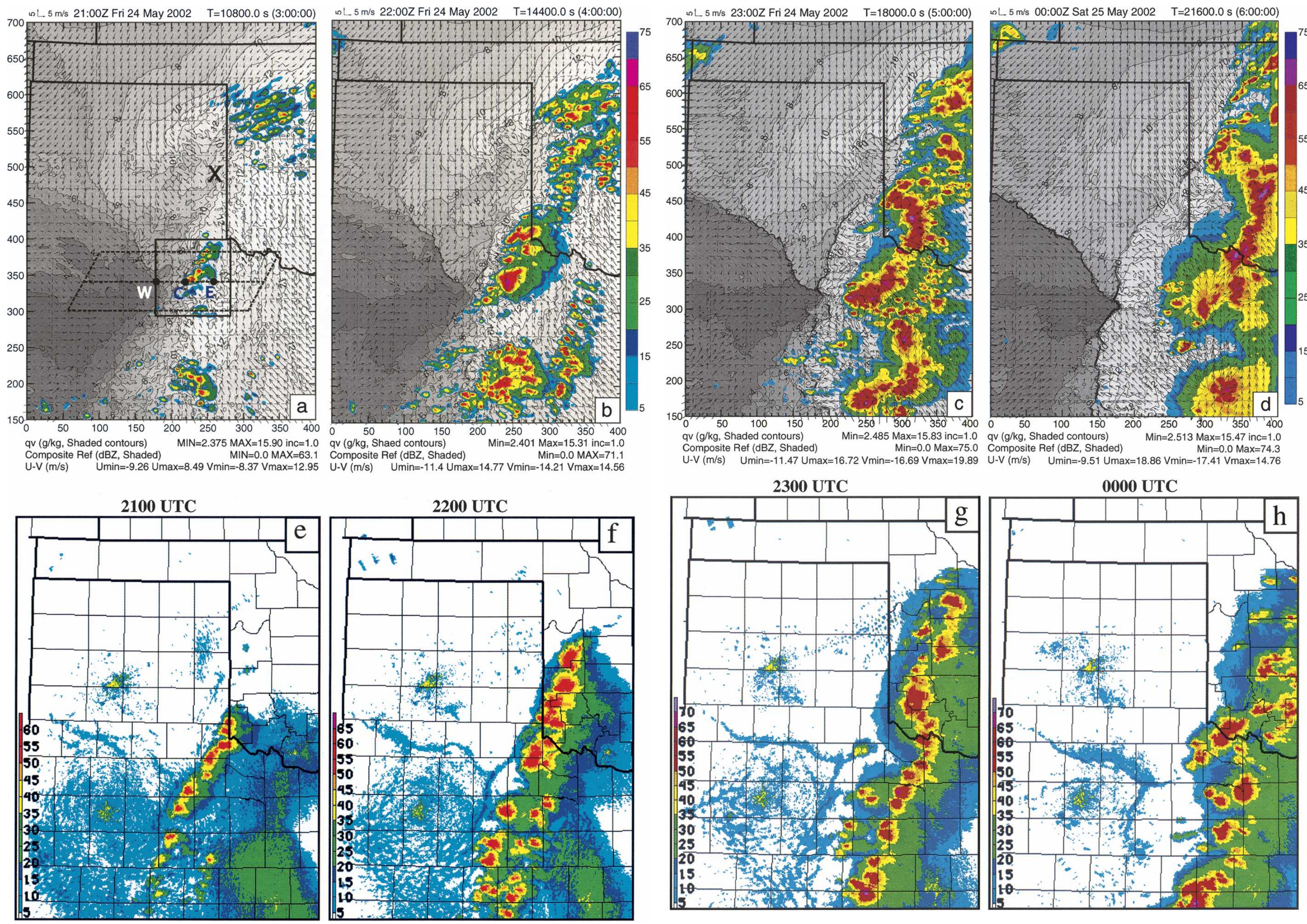

FIG. 6. ARPS 1-km forecast composite reflectivity fields (color) at (a) 2100, (b) 2200, (c) 2300 UTC 24 May, and (d) 0000 UTC 25 May 2002 together with the surface wind vectors and water vapor mixing ratio (shaded contours). (e)–(h) Same as (a)–(d) but for observed composite reflectivity. The observed reflectivity fields were composed from level-III composite reflectivity data from (counterclockwise) Amarillo (AMA), Lubbock (LBB), Midland (MAF), Abilene (DYX), and Frederick (FDR) WSR-88Ds. The clusters of enhanced reflectivity echoes near each radar site are due to ground clutter. Weak reflectivity echoes outside the precipitation regions are mostly returns from insects in the boundary layer. The "X" in (a) marks the "triple point" location at that time. The square box in (a) indicates the area shown in Fig. 8 and other figures. The bold dashed parallelogram in (a) indicates the area used by the along-dryline averages shown in Figs. 10 and 12. The dashed line through the center of the parallelogram is the location of vertical cross sections shown in Fig. 11.

south-central Kansas (cf. Fig. 4). The surface subsynoptic-scale cyclone was located to the west of this region of model convection, in the northeast Texas panhandle. The dryline–cold-front triple point was located to the south of the surface cyclone but to the north of initial dryline convection. The model convection in northwestern Oklahoma remained relatively weak and the region was later overtaken by the northeastward-moving storms initiated along the dryline, and such northeastward propagation also occurred in the observations (Fig. 6).

Farther south at about $y = 200$ km and east of the dryline, convection was initiated both in the model and in the observations before 2100 (Figs. 6a and 6e). The model convection was, however, too strong and had a cluster (Fig. 6b) instead of the observed line orientation (Fig. 6f). These differences amplified in the next a few hours, with the model echo showing too much forward bowing compared to observations (cf. Figs. 6c and 6g). Nevertheless, the initiation of convection along the northern portion of the dryline, the northeastward propagation of the storm cells, the southward extension of the convective line, and general eastward line propagation are remarkably realistic. The initiation of convection along the northern portion of the dryline is the focus of this study.

In Fig. 6, one noteworthy set of features present in the radar observations is a narrow band of enhanced reflectivity (often referred to as the fine line) extending eastward then southeastward in the south Texas panhandle area and another band extending more or less north–south, west of the convective line. Such fine lines are believed to be due primarily to the collection of insects at low-level convergence zones (Wilson et al. 1994). The former band propagated southward and was clearly associated with the shallow but strong cold front and at the eastern portion with a pool of cold air surging ahead of the main cold front; the north–south-oriented band was associated with the dryline, enhanced by the cold outflow propagating westward out of the convective line (Fig. 6). This outflow-enhanced zone of moisture gradient is clearly seen in the model fields also; in fact, this zone extends farther north than can be identified from the radar observations, but the section north of the cold-front–dryline intersection point is weaker because the air north of the cold front is more moist. The lack of insects behind the cold front and the fact that the convergence line there is weaker may be other reasons why that section of the convergence line is invisible to the radar. Elsewhere, the locations of the simulated zones of strong moist gradient match those of the observed fine lines very well.

At 2200, the observation shows a double-lined echo structure, with one line being directly associated with the dryline and the other located about 50 km farther east. By 2300, the eastern line has become the dominant one, with some of the cells in the western line merging into it while the others dissipate. There is some sign of the double-lined structure in the model as well. At 2200, a new line of cells is simulated by the model (Fig. 6b) east of the main line, although at a location that is about 50 km too far east. By 2300, and more so later on, the two lines in the model merge as the real ones did (Figs. 6c and 6d). In the model, the new cells to the east appear to have been triggered at the eastern edge of a wide zone of active BL eddies and HCRs that develop along and span across the dryline (Fig. 7). Such convective activities create discontinuities in the wind fields and, hence, convergence due to enhanced vertical mixing of momentum on the west side of the discontinuities. A similar mechanism is believed to be, at least in part, responsible for the development of drylines themselves (Schafer 1974).

The BL convective activities are indicated by the shaded vertical velocity (w) contours in Fig. 7 for hours 2000–2300. The BL open-cell-type convective eddies and horizontal convective rolls quickly develop after the model initial time. Active dry convection spans a width of 100–150 km on both sides of the dryline south of the cold front by 2000 (Fig. 7a). Interestingly, such eddies and rolls are also evident in the radar reflectivity observations, with clear roll-shaped organizations seen especially at the latter two times (Figs. 6f and 6g). These activities become weaker by 0000 on 25 May (Fig. 6h) due to reduced surface heating (local noon is at 1800), a change that is also observed in the model (not shown). The convective eddies and rolls are believed to be processes through which the vertical mixing and deepening of the convective boundary layers on both sides of the dryline are realized. Other observational studies on drylines (e.g., Atkins et al. 1998) have also shown that convective rolls can exist on both sides of the dryline. In the following section, we examine in more detail the period of dryline CI and the role of convective rolls and eddies in the CI process.

b. *Convective initiation and the role of convective rolls and eddies*

1) THE INITIATION OF CONVECTION

The model-predicted surface winds, water vapor mixing ratio (q_v), and composite reflectivity (Z) in an area centered near the dryline CI are shown in Fig. 8 at 15-min intervals, starting from 2000. The corresponding observed images of Z are also shown in the figure. As seen in the q_v fields, the zone of strong moisture gradi-

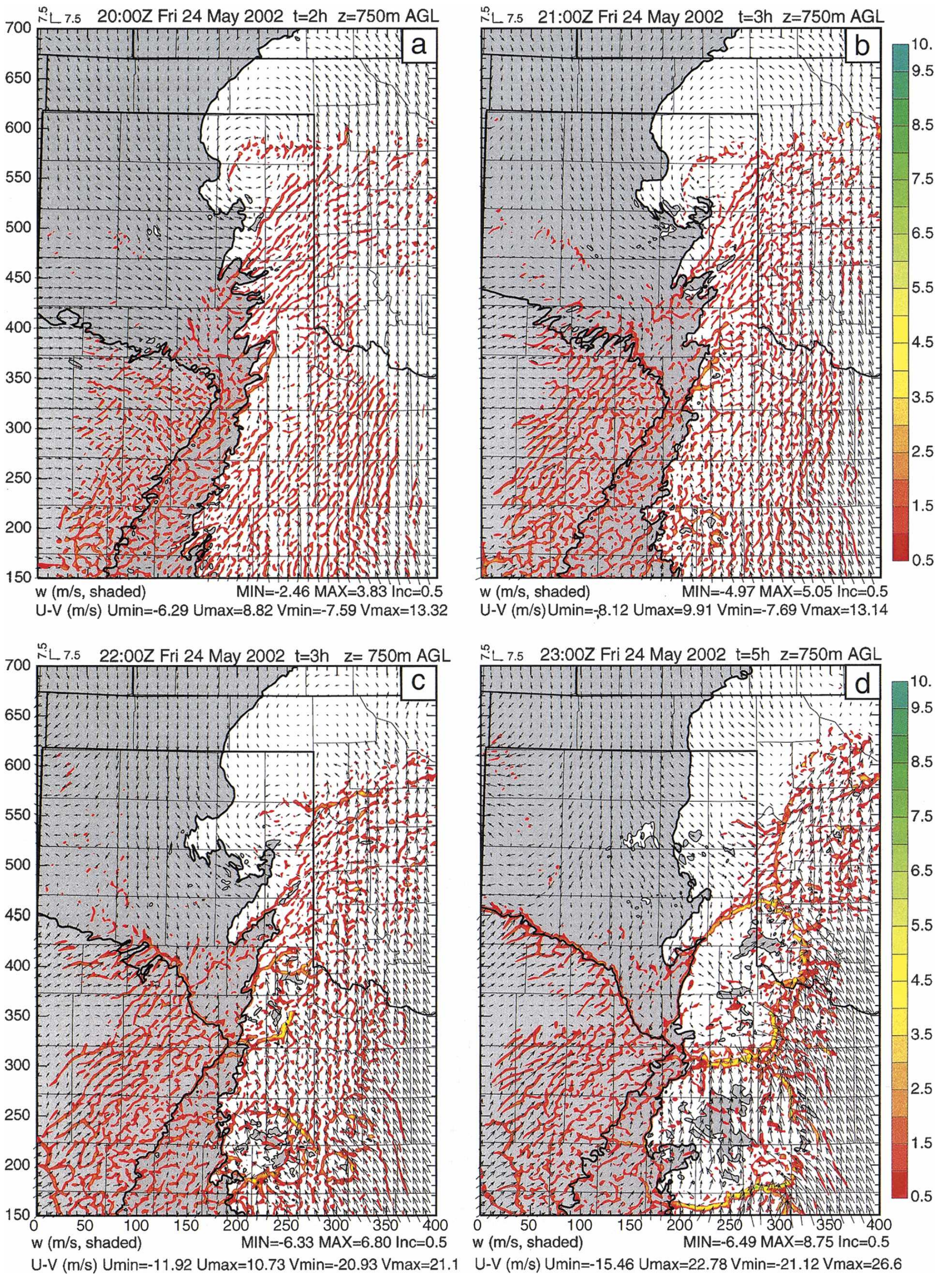

FIG. 7. The model-simulated vertical velocity fields (color shading, only positive values are shown) and horizontal wind vectors (plotted every 10th grid point) at 750 m AGL, at (a) 2000, (b) 2100, (c) 2200, and (d) 2300 UTC 24 May 2002, corresponding to model times of 2, 3, 4, and 5 h, respectively. Regions with q_v less than 8 g kg^{-1} q_v are shaded gray. The 8 and 4 g kg^{-1} q_v contours are shown in thick lines.

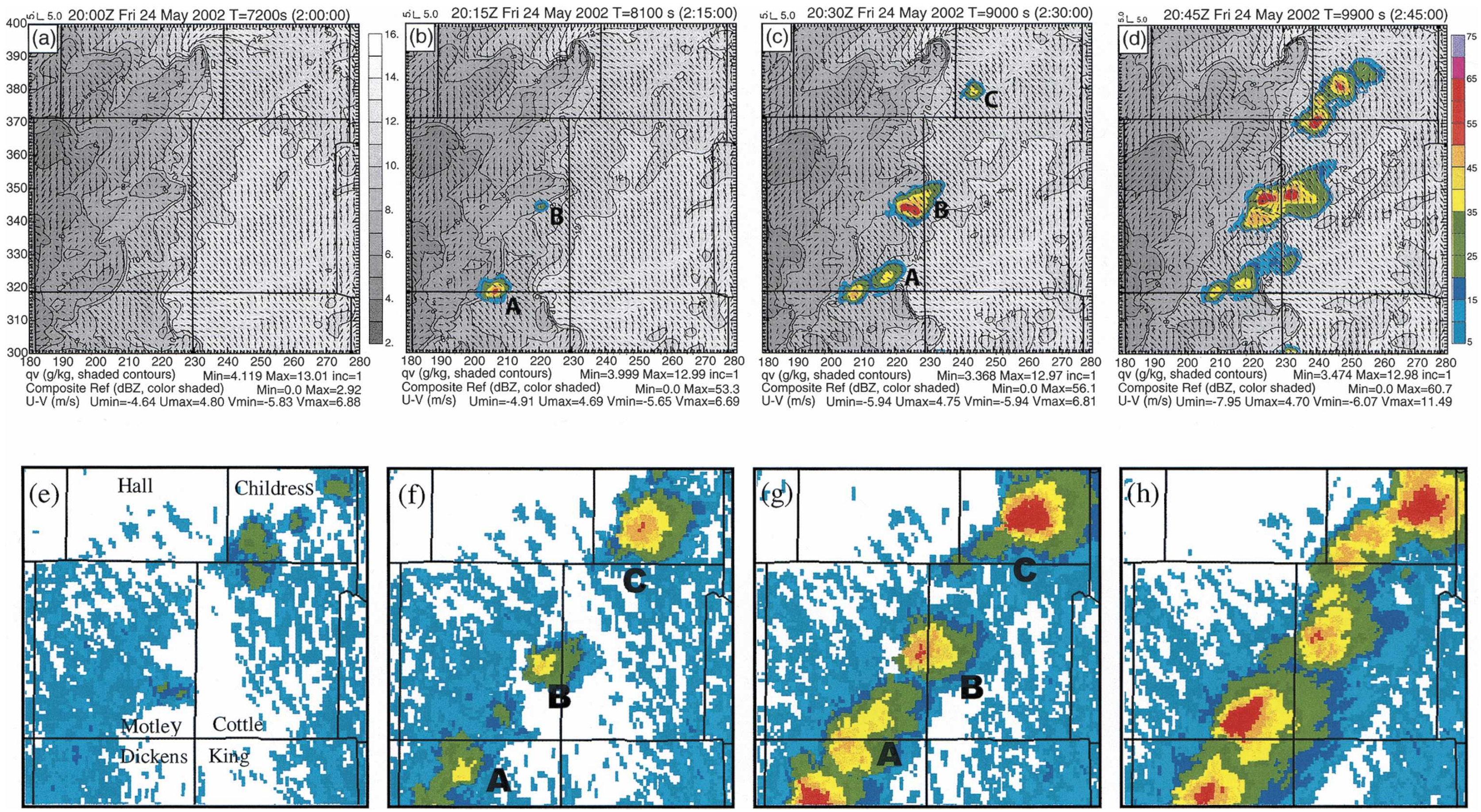

FIG. 8. (a)–(d) Model-simulated q_v (g kg^{-1}, shaded contours), wind (vectors) at 10 m AGL, and composite reflectivity (color) 15 min apart starting at 2000 UTC 24 May 2002, which corresponds to 2 h of model integration. Wind vectors are plotted every other grid point. (e)–(h) The observed composite radar reflectivity at the corresponding times. Several counties are labeled in (e). The plotted domain corresponds to the square box drawn in Fig. 6a.

ent, or the dryline, is oriented roughly along the NE–SW diagonal of the plotting domain and this zone of strong gradient has a width of about 50 km. Note that this plotting domain does not cover the clear-air echo depiction of the dryline–cold-front intersection located farther north during this period.

At 2000, observed reflectivity echoes greater than 20 dB*Z* show up for the first time along the dryline in Childress county (Fig. 8e), and the echo intensity reaches 50 dB*Z* by 2015 (Fig. 8f). These echoes correspond to the first observed storm that developed along the dryline. By 2015, other cells have developed farther south along the dryline (Fig. 8f) and these cells grow in intensity and propagate northeastward, following the lower-to-mid-tropospheric winds. We point out that at 2000, and in several volume scans that follow, the radar observations show a SW–NE-oriented and a SSW–NNE-oriented thin line intersecting each other about two counties, or 100 km, north of the domain shown in Fig. 8e, slightly to the NW of Shamrock (see city location in Fig. 1). This intersection region was the focal point of an array of instruments, including multiple-Doppler radars and aircrafts, during the IHOP field experiment (Weckwerth et al. 2004). Unfortunately, the initiation of the strongest convection occurred outside the main area of intensive observation. This points to the difficulty of forecasting the exact location of CI.

Storm initiation along the dryline predicted by the model was slightly delayed. At 2000, no radar echo exists (Fig. 8a) in the model. The first significant echo (denoted cell A) at the ground level appears between this time and 2015, at a more SW location, located at the border of Motley and Dickens Counties (Fig. 8b). This cell matches well the location (to within 10 km) of the observed cell at the southern end of the line of cells (the one in Dickens Country) at this time, but the storm farther north (cell C) did not develop in the model until 15 min later (Fig. 8c). In general, the model-predicted storms are delayed by about 15 min, as evidenced by the fact that the model simulation at 2030 (Fig. 8c) matches the radar observation at 2015 (Fig. 8f) better than that at the same time (Fig. 8g), especially in terms of the number of discrete cells that are present. By 2045, at each of the three areas, new cells have been created in the model. The presence of multiple cells in each group is also evident though less clear in the observations at 2030. The regeneration of new cells will be discussed in detail in Part II. As was observed, the model did not initiate convection at the triple point, which is located north of and outside the domain plotted in Fig. 8.

2) Structure and evolution of HCRs and OCCs at CI

Atkins et al. (1998) showed clear examples of HCRs in the environment of a dryline using WSR-88D and aircraft data. Hane et al. (2001) observed two thin lines immediately to the west of a dryline and suggested that they were due to HCRs. While the environmental conditions based on nearby soundings seemed favorable in that case, the available data were not enough to identify them with certainty. Wakimoto et al. (2006) point to the presence of cellular structures in the reflectivity field seen by an airborne radar flown at 600 m AGL in the current case, during the hour proceeding CI. A wavy pattern of thin lines is reported by them and is suggested to be the result of HCRs interacting with the dryline.

Our complete model output fields allow us to examine in detail the location of CI relative to the q_v boundaries and to boundary layer eddies and rolls, and to understand the initiation mechanism. Figure 8 shows that the storms form close to the eastern edge of the zone of strong q_v gradient, or close to the western edge of the moist air mass that came from the south-southeast, originating from the Gulf of Mexico. The initial cells are all close to the sharp convergence boundary between the southeasterly flow and the generally westerly flow west of the boundary (Figs. 8b and 8c). There exist significant small-scale variabilities in the q_v and wind fields along the dryline, and these variabilities are the results of boundary layer HCRs or the less organized open boundary layer convective cells (OCCs).

The structure of the OCCs and HCRs are more clearly revealed by the near-surface (~30 m AGL) moisture convergence fields shown in Figs. 9a–c (the pattern of this low-level convergence field closely matches that of the *w* field at the middepth of the mixed layer, located at 750 to 1 km AGL). Also shown in the plots are the wind vectors, q_v, vertical vorticity, and composite reflectivity at the same level. They are plotted for 2004, 2015, and 2027 UTC 24 May 2002, the times when 10–20 dB*Z* contours of composite reflectivity associated with storm cells A, B, and C, respectively, first appear. Storms A and B (Figs. 9a–c) are located almost directly (though not exactly) over regions of strong surface convergence locally enhanced by the upward branch of circulations of the HCRs immediately west of dryline. The situation is similar for storm C except that it is located farther east away from the low-level convergence maximum. The connection of these cells with the low-level convergence maxima will be analyzed in more detail in Part II.

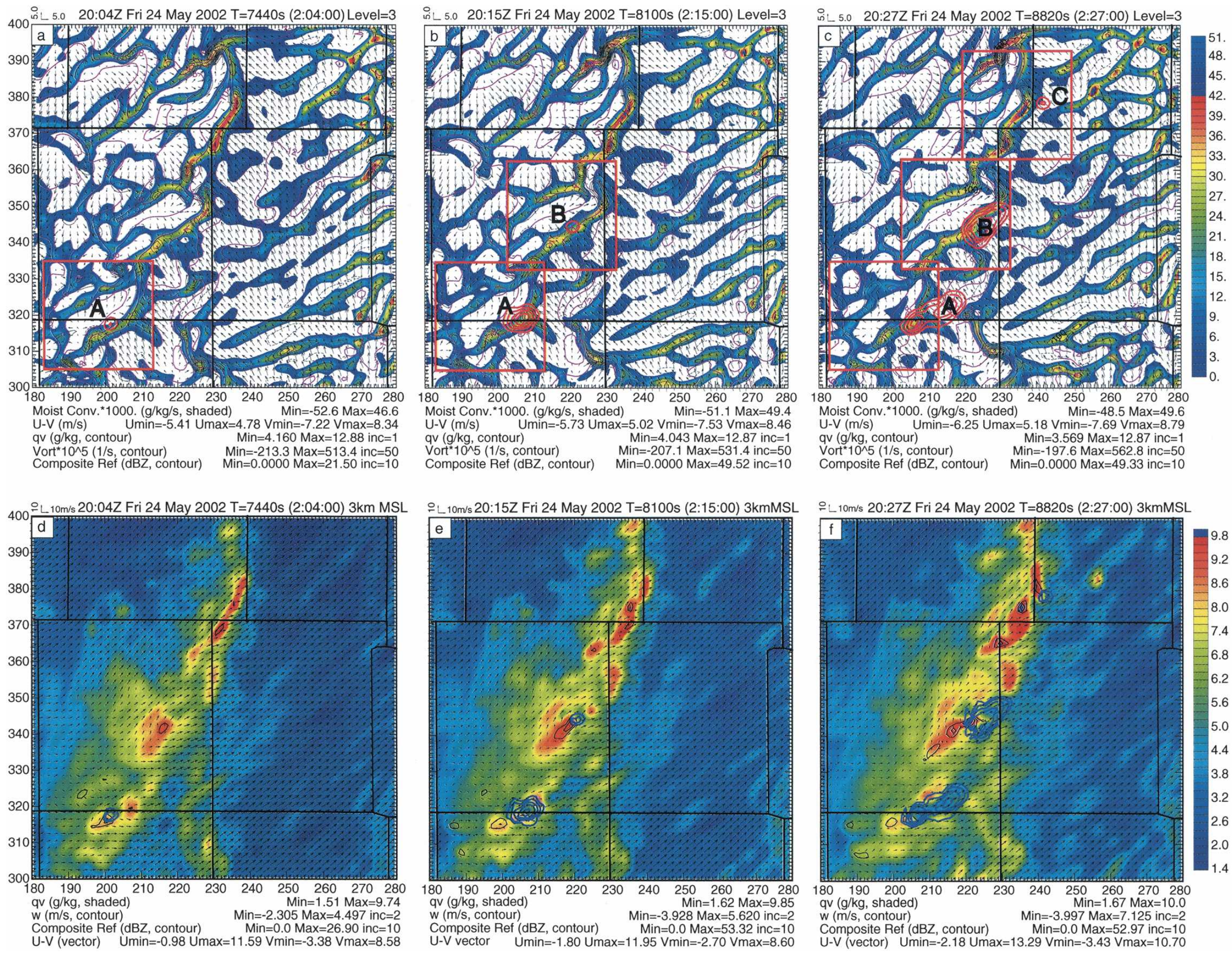

FIG. 9. (a)–(c) Model-simulated near-surface (30 m AGL) moisture convergence fields (color shading, values amplified by a factor of 1000, and only positive values shown), the horizontal wind vectors (vector key shown in the plots, m s^{-1}), the q_v field (thin contours in magenta), the vertical vorticity in thin black contours (amplified by a factor of 10^5), and the composite reflectivity in thick bright red contours, at 2004, 2015, and 2027 UTC 24 May 2002. These times correspond to the minutes that 10–20-dBZ composite reflectivity contours first appear for storm cells marked as A, B, and C in the figures, respectively. A 2D nine-point smoother was applied to all fields before plotting. (d)–(f) The model q_v (color shading), the vertical velocity (black contours), and composite reflectivity (thick blue contours) fields at 3 km MSL. No smoothing was applied before plotting. An enlarged view of the boxed regions in (a)–(c) is shown in Fig. 3 of Part II.

In Figs. 9d–f, the model-predicted q_v (color shading), w (black contours), and composite reflectivity (thick blue contours) fields at 3 km MSL are plotted, for the three times given above. The 3-km level is above the mixed-layer top at a distance from the dryline convergence zone, but is below the elevated mixed-layer top within the convergence zone (cf. Fig. 10). The elevated top in the latter case is clearly indicated by the increased moisture values in the zone at this height level.

Figure 9 also shows that there is a vertical velocity maximum at 3 km AGL that is essentially over the low-level convergence maximum each time one of the cells is initiated. The radar echoes, after they form, generally spread northeastward, in the direction of midlevel winds. These echoes appear anchored at the low-level initiation points and spread with time like a smoke plume. This behavior indicates sustained low-level lifting, at least during this period when the lifting is not interrupted by the formation of downdraft and cold pool.

On the east side of the dryline, the surface wind is south-southeasterly and the 3 km MSL winds are southwesterly, giving a wind shear vector in the mixed layer that points in the east-northeast direction. Clearly, the HCRs in this region are aligned along the direction of the low-level shear vector, which is consistent with the theory of HCRs (Kuettner 1959; Etling and Brown 1993).

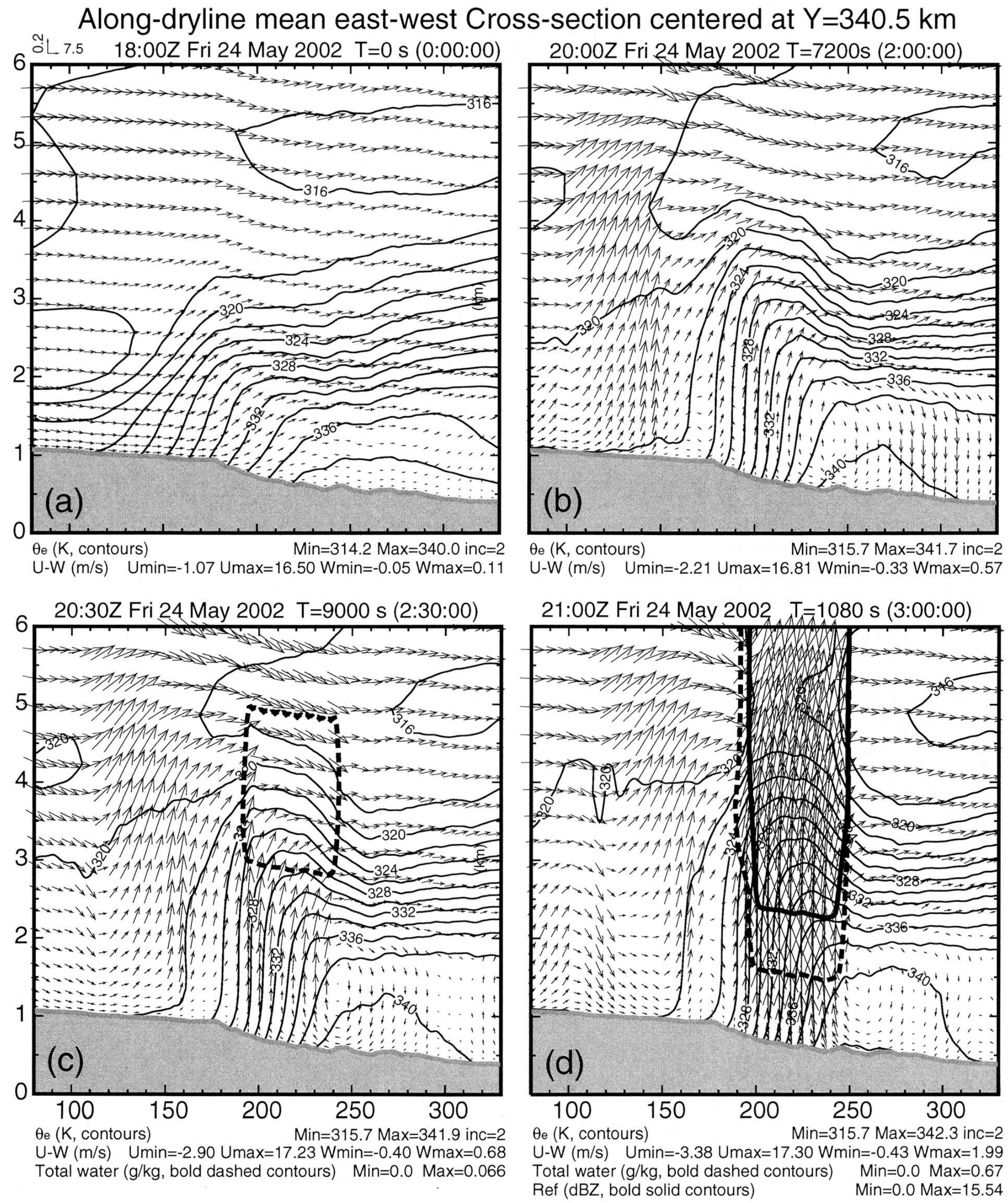

FIG. 10. Equivalent potential temperature, θ_e (contours, K), wind vectors (m s^{-1}), the 0.01 g kg^{-1} total water–ice condensate contours outlining the cloud (thick dashed contours, appearing somewhat like parallelograms), and the 5-dBZ reflectivity contours (thick solid contours), averaged in the along-dryline direction over an 80-km distance, for (a) 1800, (b) 2000, (c) 2030, and (d) 2100 UTC. The averaging is performed on east–west cross sections of 250-km width; the averaging patch is centered at x = 205 km and y = 340.5 km, and its location is shown by a parallelogram in Fig. 6a.

East of the dryline, the simulated mixed-layer depth is about 1.5 km (cf. Fig. 10). The wavelength or the distance between consecutive roll updrafts (or low-level convergence bands) on the east side away from the dryline (near the eastern boundary of the plotted domain) is between 5 and 10 km, giving roll aspect ratios (the ratio between roll wavelength and CBL depth) of between 3 and 7. They are slightly larger than the aspect ratios of 2 to 4 that are typically observed over land (Weckwerth et al. 1997; Young et al. 2002) as well as predicted by theory (Asai 1970, 1972; Brown 1980; Etling and Brown 1993) but similar to those obtained by Peckham et al. (2004), who simulated HCRs associated with a dryline under idealized conditions, also using a 1-km horizontal resolution. The relatively coarse horizontal resolution may have limited the model's ability to resolve rolls of shorter wavelengths, but the general characteristics of the resolved rolls appear realistic.

Immediately east of the main surface convergence line, in a zone 50 km wide, the convective cell or roll activity is clearly weaker (Figs. 7a and 9). It is believed that the boundary layer return circulation from the enhanced ascent in the convergence zone significantly suppresses such activity, as will be seen more clearly in the vertical cross sections presented later. The presence of descending motion on the east side of drylines has been discussed in, for example, Hane et al. (2001). A recent observation by Fovell et al. (2004) that new cells forming ahead of squall lines tend to do so tens of kilometers ahead of and away from the line suggests a similar effect at play. The significance of this observation is that the presence of this zone of damped roll activity would prevent the HCRs that form on the east side from interacting with the primary dryline convergence boundary (PDCB) and from modulating the CI. Here, the PDCB is defined as the convergence boundary between the generally southeasterly moist flow on the east side and generally westerly dry flow on the west side. More precisely, the PDCB is the eastern edge of the dryline transition zone, typically 50–100 km wide, that contains most of the moisture gradient (see also the conceptual model proposed in Part II). In our case, this transition zone lies roughly between the 4 and 8 g kg^{-1} specific humidity contours (Fig. 7). The convergence zones or bands due to cells and rolls are referred to as secondary zones or boundaries. Since a significant mean boundary layer wind component is directed toward the convergence line on both sides, the HCRs farther east generally propagate toward the PDCB but are suppressed when they get close to the PDCB. So in a sense, there exists a "shield" on the immediate east side the surface convergence boundary to these eastern HCRs that prevents them from directly interacting with the PDCB.

To the west of the PDCB, the boundary layer rolls exhibit more of a structure of elongated OCCs (Figs. 9a–c and 7). OCCs are characterized by a region of relatively weak descending motion that is surrounded by a narrow perimeter of ascending motion. The descending motion within these cells is clearly shown by the rather strong surface divergence and narrow zone of convergence in between these cells. A closer examination of the divergent winds within the elongated OCCs immediately west of cells A and B (Fig. 9b) reveals that the northeastward spreading winds are stronger than the southwestward spreading ones. We argue that downward transport of southwesterly momentum in these regions causes this asymmetry. Within the OCCs farther to the northwest, northwesterly winds are stronger. This is because this region is actually located within the northwesterly flow coming from the cold front (cf. Figs. 6a and 6e at a slightly later time, and Fig. 7 at 750 m AGL). The main cold front, especially its eastern portion close to the original cold–dryline intersection point ("X" in Fig. 6a), remains farther north, however (see wind vectors in Fig. 7).

Observational studies have revealed that HCRs often evolve into OCC structures (Agee et al. 1973) during the afternoon (Sykes and Henn 1989; Weckwerth et al. 1997; Weckwerth et al. 1999) and such a transition usually occurs when the convective instability increases and the vertical wind shear within the CBL decreases. Such conditions are present on the west side of the PDCB, where a stable cap is absent and the CBL is deeper. Further away from the PDCB toward the west, the HCR structures dominate, as can be seen in Fig. 7.

Near the PDCB, the open convective cells appear more aligned in the direction of the PDCB and therefore look more like HCRs, and the interaction of these elongated cells with the PDCB establishes several narrow bands of strong convergence (Fig. 9). These bands are at a roughly 25° angle with the mean direction of the PDCB, creating significant along-line variability. A careful look at Figs. 9a–c and at the location of the initial convective cells reveals that the preferred locations for the initiation of convection lie, especially for cells A and B, at the middle portion of the strong convergence bands. This is so because surface convergence and, therefore, upward lifting tend to be strongest there due to essentially band-perpendicular surface winds on both sides. Toward both ends of the convergence band, the flow on the west side becomes more parallel to the band, due to the divergence pattern to its west. For storm C, closed contours of Z first appeared about 5 km to the northeast of the maximum surface convergence center associated with a surface convergence band. A more detailed analysis of the relationship between the first echoes and the low-level convergence forcing is given in Part II.

c. The structure and evolution of the dryline and boundary layer

1) ALONG-DRYLINE MEAN AND REGULAR VERTICAL EAST–WEST CROSS SECTIONS

To better understand the evolution of the general structure of the dryline and of the boundary layer on both sides, we plot east–west vertical cross sections created by averaging over a distance along the direction of the dryline, which we call along-dryline-mean cross sections. We also plot the regular cross sections through the center of the averaging domain, which is shown by the parallelogram in Fig. 6a. The distance over which the averaging is performed is 80 km, and it is centered at $y = 340.5$ km (see Fig. 6a). The averaging occurs along the terrain-following model surfaces; it is reasonable to assume, according to Fig. 1, that the terrain variation in the along-line direction is small. The averaging filters out most of the details associated with the HCRs and OCCs and highlights the effects of dryline circulations on the mesoscale as well as the mean effect of boundary layer eddy mixing.

Figure 10 shows the mean wind, equivalent potential temperature, θ_e, and the cloud and precipitation regions at 1800, 2000, 2030, and 2100, corresponding to, respectively, the initial condition time, the time shortly before first radar echo associated with the dryline CI, the time shortly after the development of cells A and B, and the time when a number of storm cells are fully developed. We can see that at 1800, the top of the moist (or high θ_e) layer, defined by the 322-K θ_e contour, in the dryline convergence region, is at roughly the 2.8-km level. The flow from the west of the dryline generally runs over the moist air, which converges from the east at the low levels. By 2000, an upward "bulge" of high θ_e has developed in the dryline zone, with a westward tilting axis with height. By this time, the 322-K $\theta_{e,}$ contour has reached a height of 3.7 km, an increase of nearly 1 km. The vertical motion at the dryline is significantly enhanced, increasing from a mean value of about 0.1 m s^{-1} at 1800 to about 0.5 m s^{-1} at 2000, and the main ascending motion is located within the zone of strongest horizontal moisture gradient and extends to about 2.5 km AGL. A significant portion of this vertical motion originates from the moist side of the dryline (Figs. 10b and 10c) and is responsible for the upward moisture bulge. Also of interest is the clearly defined, rather broad (over 50 km), region of downward motion of more than 0.25 m s^{-1} within the boundary layer east of the dryline at 2000, which becomes narrower by 2030. This is clearly the forced descent in response to the strong ascent at the dryline, and it, together with the dryline ascent, forms a closed vertical circulation. Such a descent was speculated upon earlier and is confirmed here as the cause of eddy suppression in a zone of about 50 km wide immediately east of the PDCB (cf. Fig. 7a).

At 2000, the dry air from the west continues to rise and flow over the moist air, and the ascending path is steeper as the layer of moist air becomes deeper (Fig. 10b). Also worth noting in Fig. 10b and at later times is the strong ascent that develops tens of kilometers upstream (west) of the moisture boundary. A careful examination of the low-level flow fields (e.g., Fig. 6 and the fields at earlier times, and Fig. 7) reveals that this ascent was associated with a surface convergence boundary set up by a pool of cold air spreading southward from the cold front (cf. Fig. 6a) and this pool of air was actually spreading in both east- and westward directions, creating another moisture boundary west of the dryline (Figs. 6a and 6b) within the northern portion of the averaging domain. This moisture boundary is indicated more clearly in Fig. 7 by the 4 g kg^{-1} specific humidity contours. The westward spreading is also responsible for the reduction in westerly momentum in this region, seen in Fig. 12b, which shows the u difference between 2030 and 1800. This "wedge" of cold air turned the low-level flow immediately west of the main dryline convergence line predominantly northwesterly. Indications of such a background flow are evident even in the presence of significant boundary eddy and roll activities. For example, the northwesterly component of surface divergent flow within the OCCs in the northwest portion of Fig. 9b is much stronger, while in the southwest part of the domain, the southwesterly component is stronger.

After 2000, the height of the 322-K θ_e contour increases further, to 3.9 km at 2030 and to above 4 km by 2100. At 2030, clouds are present in the mean cross section (Fig. 10c), and by 2100, significant precipitating hydrometeors have also developed, giving mean Z values above 15 dBZ (Fig. 10d). By this time, the full development of convective cells gives a mean vertical velocity of nearly 2 m s^{-1} in a zone of about 50 km wide and the 320-K θ_e contours now extend above the 6-km level, the top of the plotting domain. Indications of the downward transport of westerly momentum by HCRs is visible west of $x = 150$ km and below 3 km in Fig. 10d.

The actual development of individual cells occurs in a much narrower zone than indicated by the mean fields. Figure 11 shows the cross section through the center of the averaging domain (at $y = 340.5$ km; cf. Fig. 6a). We can see that the general structure of the dryline is similar to that seen in Fig. 10, but the additional small-scale features seem to be responsible for triggering the convection. The figure also shows wave patterns of w throughout the depth of the plotting domain, and the pattern reflects roll and eddy activities at the levels and gravity wave activities above. The evolution of the general structure, including the deepening of the moist boundary layer, in response to the broader

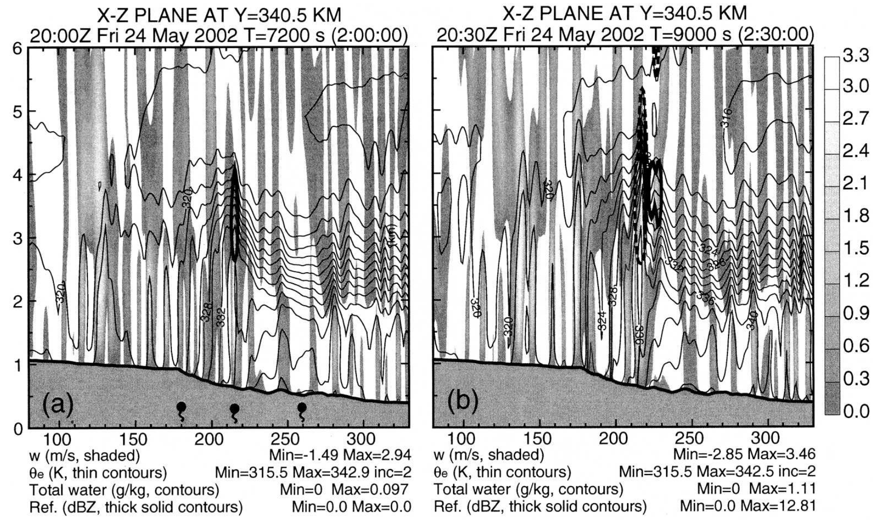

FIG. 11. Equivalent potential temperature (contours, K), gray-shaded w contours (only positive values are shown, m s^{-1}), the 0.01 g kg^{-1} total water–ice condensate contours outlining the cloud (bold dashed contours), and the 5-dBZ reflectivity contours (bold solid contours), in an east–west cross section through the center of the averaging patch used in Fig. 10 (at y = 340.5 km), for (a) 2000 and (b) 2030 UTC. See also the caption of Fig. 6 on the averaging domain. The three balloon symbols in (a) indicate the locations (at x = 180, 215, and 260 km and y = 340.5 km) of extracted soundings to be shown in Figs. 13–15.

dryline convergence forcing is, however, also essential for CI. It preconditions the lower atmosphere in which additional lifting by HCR convergence pushes the air parcels above their level of free convection (LFC).

In addition, in Fig. 12, we plot for 2030 the mean cross sections of water vapor q_v, horizontal winds, east–west wind component u and its increment since 1800, and potential temperature θ. The q_v field (Fig. 12a) exhibits a similar bulge as the θ_e field (Fig. 10c), and horizontal wind barbs show veering of winds with height on the east side of the dryline and a deep layer of winds with significant direction changes (due to eddies) to the west (Fig. 12a). Total θ (Fig. 12c) shows a well-mixed boundary layer below 3.5 and 2 km, respectively, to the west and east of the dryline. It also shows the presence of a shallow and weak (about 0.5 K over 500 m) superadiabatic layer on the east side. The suppression of eddy activities in the region discussed earlier must have helped maintain this superadiabatic lapse rate. The features of u momentum and its change in Fig. 12b were discussed earlier.

2) SKEW T DIAGRAMS OF EXTRACTED SOUNDINGS

The structure and evolution of the boundary layer and the associated convective instability are further revealed by soundings extracted from the instantaneous and along-dryline mean model fields. Soundings extracted from three locations, one on the west side, one on the east side, and one on the dryline, as indicated by the black dots labeled "W," "E," and "C" in Fig. 6a, respectively, are plotted in Figs. 13–15 for the initial time (1800) and the hours before, near, and after dryline CI. The locations are on the central line of the averaging domain used earlier, and corresponding to the locations indicated by "balloon" symbols in Fig. 11a. As can be seen from Fig. 11a, clouds were formed in the model at location C on the dryline at 2000. In fact, this location (x = 215 km and y = 340.5 km) is almost exactly the location where cell B is triggered.

Figure 13 shows the skew T plots of soundings extracted at the dryline location C from the initial time 1800 through 2100 at 1-h intervals. At 1800, C is located near the eastern edge of the surface moisture gradient zone; the surface air is therefore rather moist with a mixing ratio of 11.5 g kg^{-1}. The BL of about 1.5 km deep is well mixed below 800 hPa. Above 800 hPa exists a stable layer about 50 hPa deep (Fig. 13a) and this stable layer creates a 49 J kg^{-1} CIN for surface parcels. The air becomes much drier starting at the bottom of the stable layer, reflecting its origin from west of the dryline. Such a vertical sounding is very typical of the environment on the moist side of drylines (e.g., Hane et al. 1997).

The mixed layer deepens in the ensuing hours; by 1900, the mixed-layer top is increased from the 800- to 850-hPa level as the potential temperature in the layer

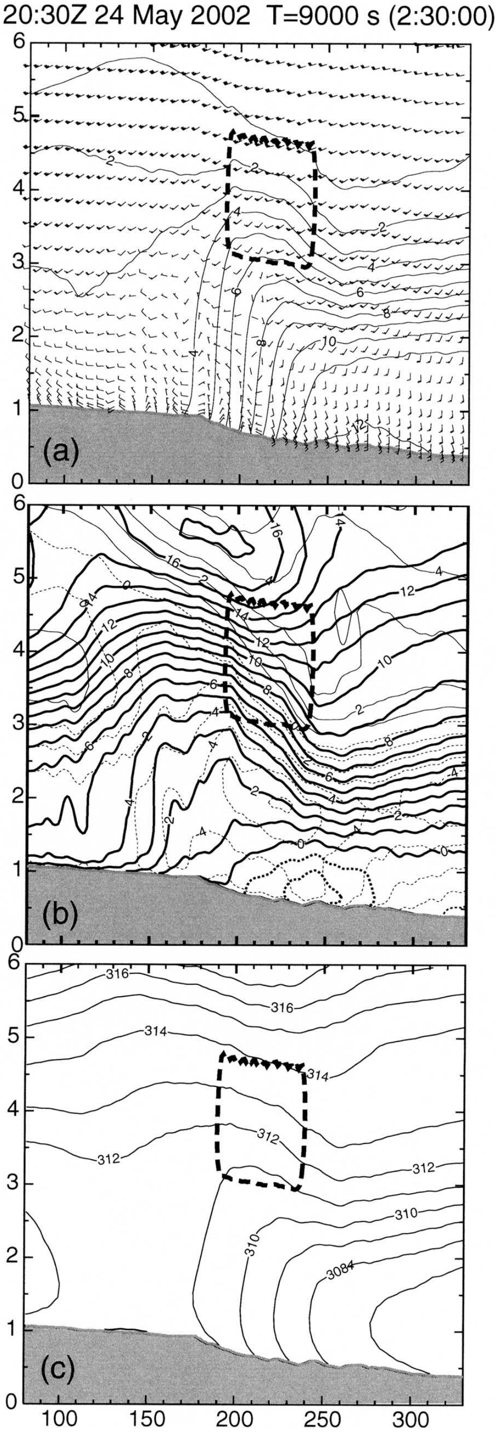

FIG. 12. Plots for fields averaged in the same way as those in Fig. 10, at 2030 UTC. The fields are (a) water vapor mixing ratio, q_v (thin contours, g kg^{-1}), and horizontal wind barbs (one full barb = 5 m s^{-1}), (b) east–west wind component, u (thick contours, m s^{-1}), and the increment of u from its value at 1800 UTC (thin contours, with negative contours dashed), and (c) total potential temperature, θ (K, thin contours). The bold "parallelograms" are the 0.01 g kg^{-1} total water–ice condensate contours outlining the cloud.

increases by a few degrees kelvin. The BL moisture has become better mixed with the surface mixing ratio reduced to 10 g kg^{-1} (Fig. 13b). A small amount of CIN remains and no saturation is present at this time. By 2000 (Fig. 13c), the neutrally stable mixed layer has been extended above 700 hPa and the water vapor is fully mixed in the BL. Saturation has occurred within the 700–650-hPa layer and the LFC is reached freely by the surface parcel at 715 hPa, or about 3 km MSL, as CIN is reduced to zero. The first sign of saturation actually occurs at 1954 (not shown). This saturation layer matches well the cloud found in the vertical cross section in Fig. 11a, and the cloud is ready to "fire off" given that the LFC has been reached and the cloud extends above the LFC. This indeed happens in the model (Fig. 11), at the time and location that are very close to reality. By 2100, the convective cells that develop at location C have mostly moved off to the NE, but C remains within the western edge of the reflectivity region (Fig. 6a); a saturated layer therefore remains in the skew T diagram (Fig. 13d). The saturated layer extends up to 550 hPa between 2000 and 2100 at location C.

Figure 14 shows the soundings at 1800 and 2100, taken at locations W and E, 35 and 45 km west and east of the dryline point C, respectively. Point W is located on the western edge of the strong surface moisture gradient zone at 2100 with a surface moisture value of about 4 g kg^{-1}, while E is located inside the moist air mass. On the west side, the mixing causes surface drying of about 3 g kg^{-1} between 1800 and 2100 while surface heating increased surface temperature by 2–3 K despite intense vertical mixing. The well-mixed neutral layer extends above 600 hPa or 4.5 km MSL. The layer above has a stratification that is very close to moist adiabatic (Fig. 14c). CIN is closed to zero (-4 J kg^{-1}) and CAPE is also very small (169 J kg^{-1}) at this time and location. Even though the skew T diagram indicates that the surface parcel can reach the LCL without much difficulty, mixing and entrainment have probably prevented any clouds from forming in this dry region, even in the presence of significant HCR activities. The along-dryline-mean structure shown in Fig. 15 is very similar to the sounding structure at the current time and location, indicating that this sounding profile is representative of the dry region. The sounding is also similar to many observed soundings taken west of drylines (e.g., Hane et al. 1997).

On the east side (Figs. 14b and 14d), the mixed layer is shallower and the stable "cap" is stronger. The well-mixed layer deepens from 1800 to 2100 but remains below 800 hPa, which is below the LFC of 740 hPa (Fig. 14d). Despite the essentially zero CIN, clouds were not

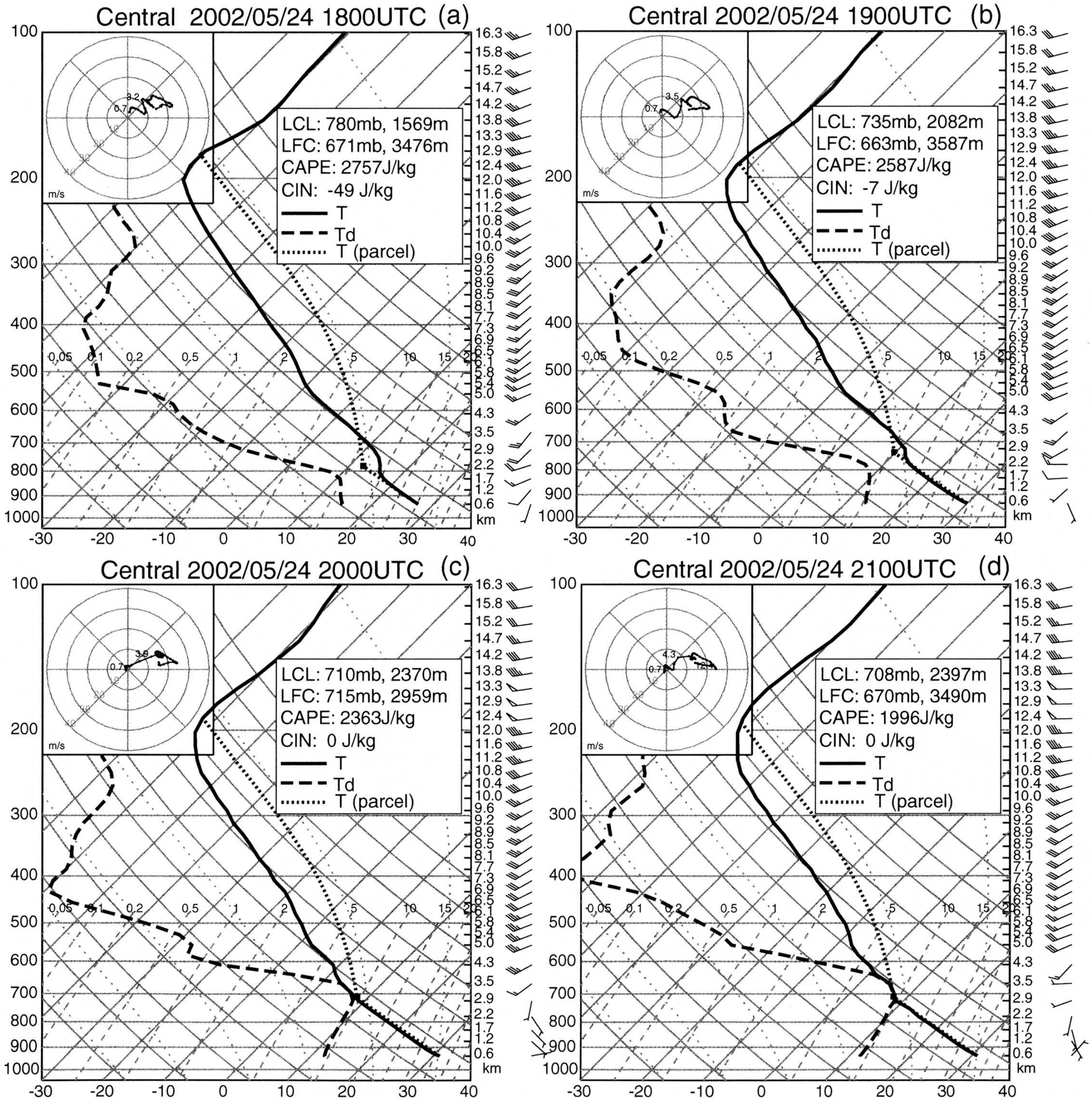

FIG. 13. Skew T plots of soundings extracted from model forecasts at the black dot location labeled "C" in Fig. 6a, at 1800, 1900, 2000, and 2100 UTC. Corresponding hodographs are plotted as inset. The sounding location is also indicated by the "balloon" at $x = 215$ km and $y = 340.5$ km in Fig. 11a.

forming at this location; the downward return circulation in this region probably helped suppress clouds. While the difference in the mixed-layer depth is also clearly seen in the vertical cross sections (Fig. 11), the skew T diagrams reveal to us more clearly the conditions and their evolution for CI.

The deepened moist layer in the dryline convergence zone and the associated creation of a deep well-mixed layer clearly contribute to the initiation of convection in the region. The actual initiation resulted from additional forcing by localized features, specifically, by localized surface convergence maxima related to HCRs, as is analyzed in detail in Part II. To lend support to this argument, we plot the along-dryline-mean soundings in Fig. 15. The averaging removes small-scale features associated with boundary layer eddies. It can be seen that, while the thermal structure of the boundary layer and the atmosphere above is generally similar to the non-

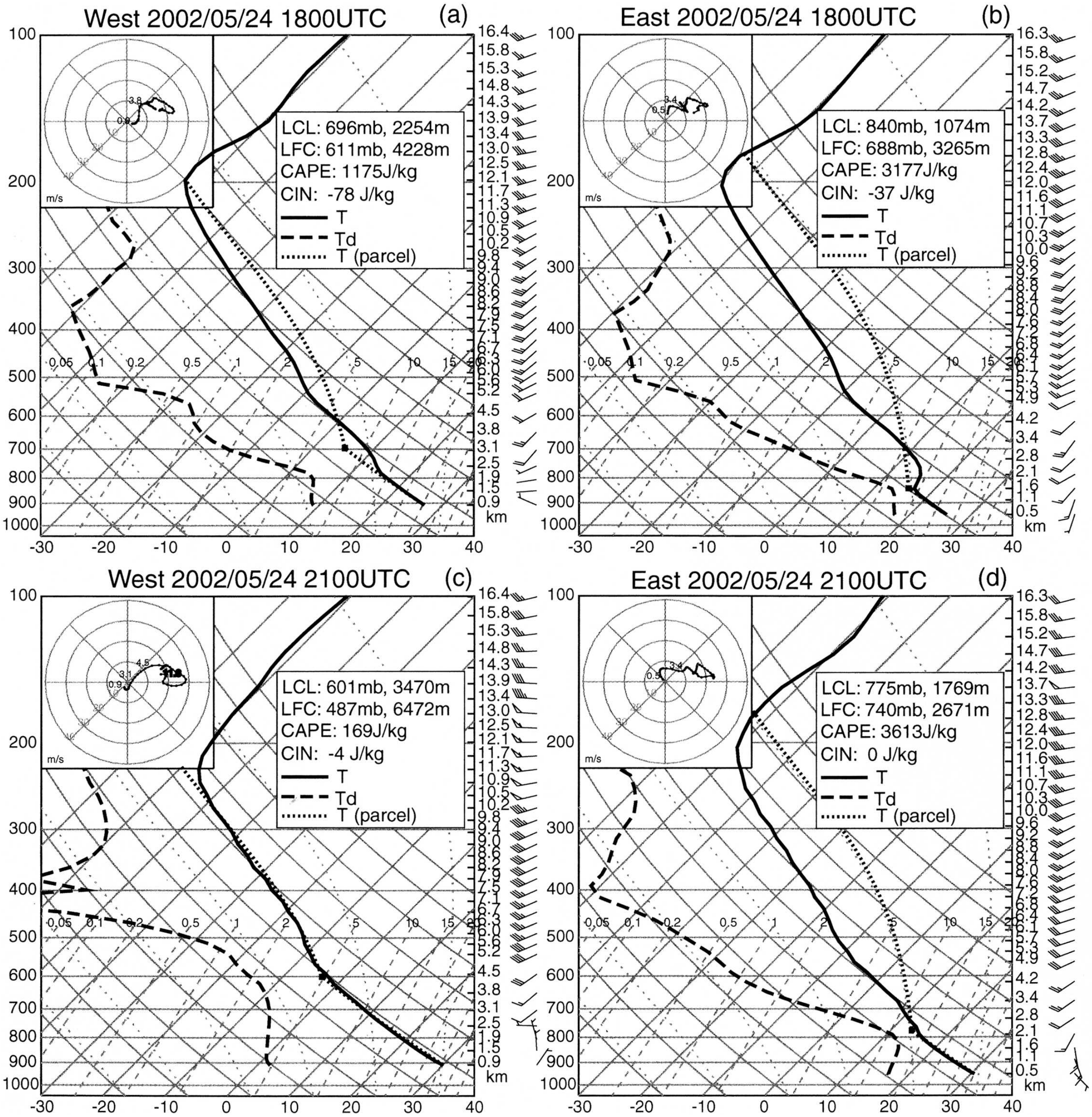

FIG. 14. Skew T plots of soundings extracted from model forecasts at the black dot locations labeled (left) "W" (west of dryline) and (right) "E" (east of the dryline) in Fig. 6a, respectively, for (a), (b) 1800 and (c), (d) 2100 UTC. The "west" and "east" sounding locations are also indicated by the "balloons" at x = 180 and 260 km and y = 340.5 km in Fig. 11a.

averaged one, saturation is not reached in the mean soundings. This implies that the mesoscale circulation associated with dryline convergence is insufficient to produce saturation in the entire 80-km-long (the north–south length of the averaging domain) zone at the dryline, at least not by this time. Along-line inhomogeneity caused localized initiation.

Finally, we note that the hodographs plotted in the above figures indicate mostly northeastward wind shear in the boundary layer, explaining the predominant SW–NE orientation of the HCRs.

5. Summary

In this study, high-resolution numerical simulations of the 24 May 2002 dryline convective initiation (CI)

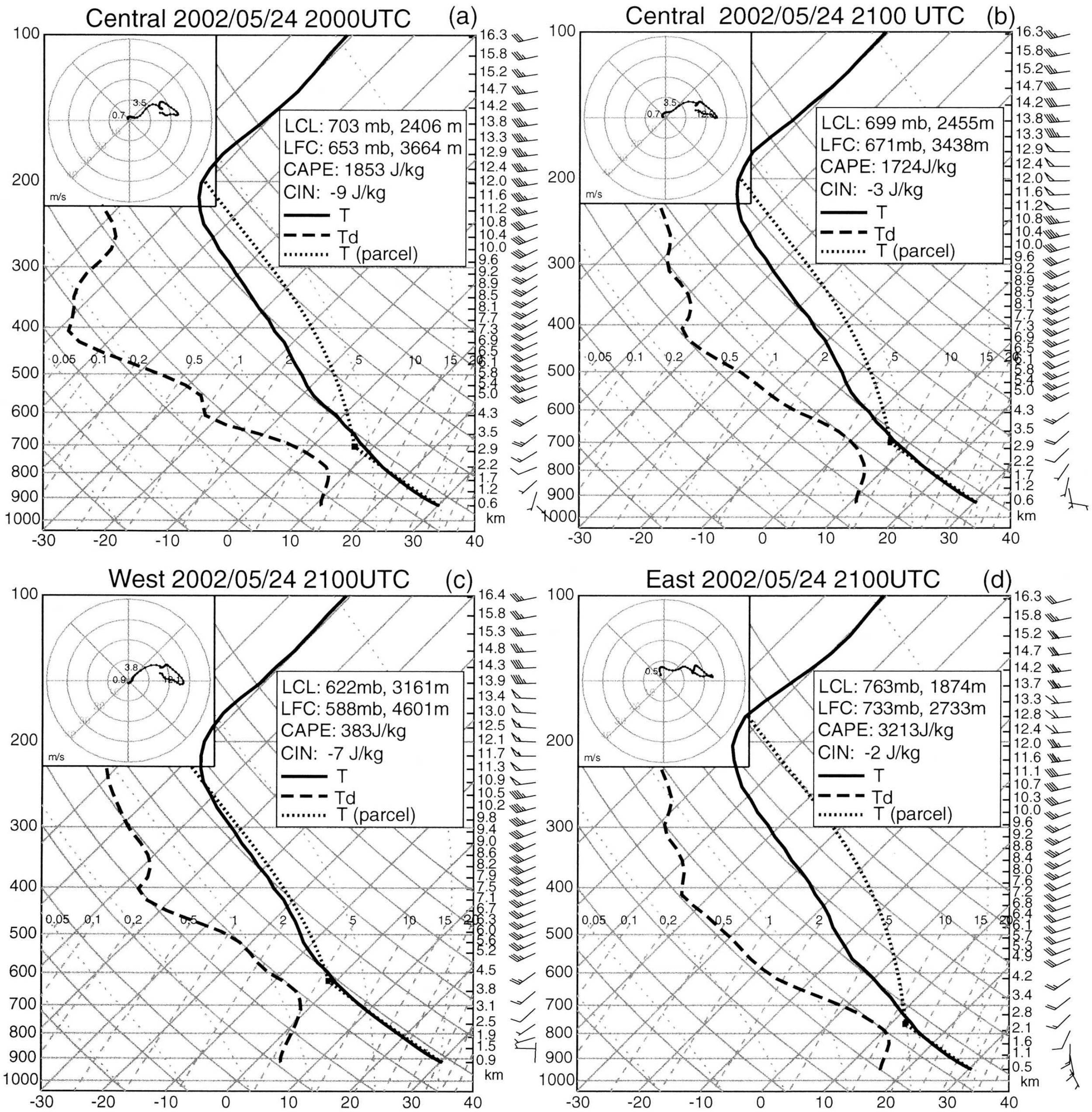

FIG. 15. Skew *T* plots of soundings extracted from along-dryline-average model forecast fields, at the black dot locations labeled "C" in Fig. 6a at (a) 2000 and (b) 2100 UTC, and (c) at the "western location" marked by "W" and (d) at the "eastern location" marked by "E" at 2100 UTC.

case observed during IHOP_2002 are performed, starting from an initial condition that assimilates routine as well as special upper-air and surface observations collected during IHOP. The simulation employs a nonhydrostatic mesoscale model, the ARPS, and its data analysis system, ADAS. The large (400×700 km^2) 1-km grid nested inside a 3-km grid is able to resolve the detailed structure of boundary layer eddies, including horizontal convective rolls and open convective cells with realistic orientations and aspect ratios. The initiation of convective storms at around 2015 is correctly predicted along a section of the dryline south of the Texas panhandle, as is the noninitiation of convection at the cold-front–dryline "triple point." The timing and location of the predicted CI are accurate to within 20 min and 25 km (about half a county), respectively. The general evolution of the predicted convective line in the 3 to 4 h that follow also verifies well.

The evolution of the mean vertical structure of the dryline is also examined. Mesoscale convergence associated with confluent flow around the dryline is shown to produce an upward moisture bulge, while surface heating and boundary layer mixing is responsible for the general deepening of the well-mixed and moist boundary layer. The top of the well-mixed neutrally stable and moist layer in the primary dryline convergence boundary (PDCB) is often half a kilometer or so higher than that to its east. These processes preconditioned the convergence zone, making it easier for surface air parcels to reach the LFC, but the mesoscale forcing by itself did not trigger the convection.

Our results suggest that additional lifting from localized forcing associated with HCRs from the west side of the PDCB and their interaction with the PDCB plays a key role in convective initiation. In addition, there exists a zone of weak boundary layer eddy activity immediately east of the PDCB, due to suppression by the descending branch of the mesoscale dryline circulation. This zone essentially “shields” the PDCB from direct interaction with the boundary layer eddies or rolls on the east side. The exact processes by which the HCRs interact with the dryline and how convective cells are initiated are analyzed in detail in a companion paper.

Finally, we note that the model simulation presented in this paper is not perfect. The model produced, near the time of main dryline CI, some spurious, scattered, though weak, convective cells in northwestern Oklahoma where strong surface convergence is found along the cold front. These cells remained relatively weak and did not seem to affect much the main cells that were initiated along the dryline to the southwest as they propagated into this region. There was also some spurious or too strong convection occurring farther south to the east of the dryline. Simulations with more frequent assimilation cycles between 1200 and 1800 are planned, which hopefully can eliminate these spurious features.

Acknowledgments. This work was primarily supported by NSF Grant ATM0129892. The first author was also supported by NSF ATM-9909007, ATM-0331594, and EEC-0313747, a DOT-FAA grant via DOC-NOAA NA17RJ1227, a grant from the Chinese Natural Science Foundation (40028504), and the “Outstanding Overseas Scholars” Award of Chinese Academy of Sciences (Grant 2004-2-7). Geoffrey Stano is acknowledged for some initial data preparation. Assistance was also provided by Keith Brewster. A Linux cluster operated by OSCER of University of Oklahoma and the NSF-supported Terascale Computing System at the Pittsburgh Supercomputing Center were used for the simulations. Much appreciation goes to Dr. Carl Hane and three anonymous reviewers whose comments improved the original manuscript.

REFERENCES

Agee, E. M., T. S. Chen, and K. E. Doswell, 1973: A review of mesoscale cellular convection. *Bull. Amer. Meteor. Soc.,* **54,** 1004–1012.

Asai, T., 1970: Stability of a plane parallel flow with variable vertical shear and unstable stratification. *J. Meteor. Soc. Japan,* **48,** 129–139.

——, 1972: Thermal instability of a shear flow turning the direction with height. *J. Meteor. Soc. Japan,* **50,** 525–532.

Atkins, N. T., R. M. Wakimoto, and C. L. Ziegler, 1998: Observations of the finescale structure of a dryline during VORTEX 95. *Mon. Wea. Rev.,* **126,** 525–550.

Bluestein, H. B., and S. S. Parker, 1993: Modes of isolated, severe convective storm formation along the dryline. *Mon. Wea. Rev.,* **121,** 1352–1374.

Bratseth, A. M., 1986: Statistical interpolation by means of successive corrections. *Tellus,* **38A,** 439–447.

Brewster, K., 1996: Application of a Bratseth analysis scheme including Doppler radar data. Preprints, *15th Conf. on Weather Analysis and Forecasting*, Norfolk, VA, Amer. Meteor. Soc., 92–95.

Brown, R. A., 1980: Longitudinal instabilities and secondary flows in the planetary boundary layer: A review. *Rev. Geophys. Space Phys.,* **18,** 683–697.

Chen, F., K. W. Manning, D. N. Yates, M. A. LeMone, S. B. Tries, R. Cuenca, and D. Niyogi, 2004: Development of high resolution land data assimilation system and its application to WRF. Preprints, *20th Conf. on Weather Analysis and Forecasting/16th Conf. on Numerical Weather Prediction*, Seattle, WA, Amer. Meteor. Soc., CD-ROM, 22.3.

Chou, M.-D., 1990: Parameterization for the absorption of solar radiation by O_2 and CO_2 with application to climate studies. *J. Climate,* **3,** 209–217.

——, 1992: A solar radiation model for climate studies. *J. Atmos. Sci.,* **49,** 762–772.

——, and M. J. Suarez, 1994: An efficient thermal infrared radiation parameterization for use in general circulation models. NASA Tech. Memo. 104606, 85 pp.

Etling, D., and R. A. Brown, 1993: Roll vortices in the planetary boundary layer: A review. *Bound.-Layer Meteor.,* **65,** 215–248.

Fovell, R. G., B. Rubin-Oseter, and S.-H. Kim, 2004: A discretely propagating nocturnal Oklahoma squall line: Observations and numerical simulations. Preprints, *22d Conf. on Severe Local Storms*, Hyannis, MA, Amer. Meteor. Soc., CD-ROM, 6.1.

Geerts, B., R. Damiani, and S. Haimov, 2006: Finescale vertical structure of a cold front as revealed by airbone Doppler radar. *Mon. Wea. Rev.,* **134,** 251–271.

Grasso, L. D., 2000: A numerical simulation of dryline sensitivity to soil moisture. *Mon. Wea. Rev.,* **128,** 2816–2834.

Hane, C. E., C. L. Ziegler, and H. B. Bluestein, 1993: Investigation of the dryline and convective storms initiated along the dryline: Field experiments during COPS-91. *Bull. Amer. Meteor. Soc.,* **74,** 2133–2145.

——, H. B. Bluestein, T. M. Crawford, M. E. Baldwin, and R. M. Rabin, 1997: Severe thunderstorm development in relation to along-dryline variability: A case study. *Mon. Wea. Rev.,* **125,** 231–251.

——, M. E. Baldwin, H. B. Bluestein, T. M. Crawford, and R. M. Rabin, 2001: A case study of severe storm development along a dryline within a synoptically active environment. Part I: Dryline motion and an Eta Model forecast. *Mon. Wea. Rev.,* **129,** 2183–2204.

——, R. M. Rabin, T. M. Crawford, H. B. Bluestein, and M. E. Baldwin, 2002: A case study of severe storm development along a dryline within a synoptically active environment. Part II: Multiple boundaries and convective initiation. *Mon. Wea. Rev.,* **130,** 900–920.

Holt, T. R., D. Niyogi, F. Chen, K. Manning, M. A. LeMone, and A. Qureshi, 2006: Effect of land–atmosphere interactions on the IHOP 24–25 May 2002 convection case. *Mon. Wea. Rev.,* **134,** 113–133.

Kuettner, J., 1959: The band structure of the atmosphere. *Tellus,* **11,** 267–294.

Lin, Y.-L., R. D. Farley, and H. D. Orville, 1983: Bulk parameterization of the snow field in a cloud model. *J. Climate Appl. Meteor.,* **22,** 1065–1092.

Noilhan, J., and S. Planton, 1989: A simple parameterization of land surface processes for meteorological models. *Mon. Wea. Rev.,* **117,** 536–549.

Peckham, S. E., R. B. Wilhelmson, L. J. Wicker, and C. L. Ziegler, 2004: Numerical simulation of the interaction between the dryline and horizontal convective rolls. *Mon. Wea. Rev.,* **132,** 1792–1812.

Ren, D., and M. Xue, 2004: A revised force–restore model for land surface modeling. *J. Appl. Meteor.,* **43,** 1768–1782.

Rhea, J. O., 1966: A study of thunderstorm formation along drylines. *J. Appl. Meteor.,* **5,** 58–63.

Schafer, J. T., 1974: A simulative model of dryline motion. *J. Atmos. Sci.,* **31,** 956–964.

Shaw, B. L., 1995: The effect of soil moisture and vegetation heterogeneity on a Great Plains dryline: A numerical study. M.S. thesis, Dept. of Atmospheric Science, Colorado State University, 93 pp.

——, R. A. Pielke, and C. L. Ziegler, 1997: A three-dimensional numerical simulation of a Great Plains dryline. *Mon. Wea. Rev.,* **125,** 1489–1506.

Stano, G., 2003: A case study of convective initiation on 24 May 2002 during the IHOP field experiment. M.S. thesis, School of Meteorology, University of Oklahoma, 106 pp.

Sun, W.-Y., and C.-Z. Chang, 1986: Diffusion model for a convective layer. Part I: Numerical simulation of convective boundary layer. *J. Climate Appl. Meteor.,* **25,** 1445–1453.

Sykes, R. I., and D. S. Henn, 1989: A large-eddy simulation of turbulent sheared convection. *J. Atmos. Sci.,* **46,** 1106–1118.

Tong, M., and M. Xue, 2005: Ensemble Kalman filter assimilation of Doppler radar data with a compressible nonhydrostatic model: OSS experiments. *Mon. Wea. Rev.,* **133,** 1789–1807.

Wakimoto, R. M., H. V. Murphey, E. V. Browell, and S. Ismail, 2006: The "triple-point" on 24 May 2002 during IHOP. Part I: Airborne Doppler and LASE analyses of the frontal boundaries and convection initiation. *Mon. Wea. Rev.,* **134,** 231–250.

Weckwerth, T. M., J. W. Wilson, R. M. Wakimoto, and N. A. Crook, 1997: Horizontal convective rolls: Determining the environmental conditions supporting their existence and characteristics. *Mon. Wea. Rev.,* **125,** 505–526.

——, T. W. Horst, and J. W. Wilson, 1999: An observational study of the evolution of horizontal convective rolls. *Mon. Wea. Rev.,* **127,** 2160–2179.

——, and Coauthors, 2004: An overview of the International H_2O Project (IHOP_2002) and some preliminary highlights. *Bull. Amer. Meteor. Soc.,* **85,** 253–277.

Wilson, J. W., T. M. Weckwerth, J. Vivekanadan, R. M. Wakimoto, and R. W. Russell, 1994: Boundary layer clear-air radar echoes: Origin of echoes and accuracy of derived winds. *J. Atmos. Oceanic Technol.,* **11,** 1184–1206.

Xue, M., and D. Ren, 2004: Testing of several recent modifications to ARPS land surface model. Preprints, *18th Conf. on Hydrology*, Seattle, WA, Amer. Meteor. Soc., CD-ROM, JP4.16.

——, and W. J. Martin, 2006: A high-resolution modeling study of the 24 May 2002 dryline case during IHOP. Part II: Horizontal convective rolls and convective initiation. *Mon. Wea. Rev.,* **134,** 172–191.

——, K. K. Droegemeier, V. Wong, A. Shapiro, and K. Brewster, 1995: ARPS version 4.0 user's guide. 380 pp. [Available online at http://www.caps.ou.edu/ARPS.]

——, J. Zong, and K. K. Droegemeier, 1996: Parameterization of PBL turbulence in a multi-scale non-hydrostatic model. Preprints, *11th Conf. on Numerical Weather Prediction,* Norfolk, VA, Amer. Meteor. Soc., 363–365.

——, K. K. Droegemeier, and V. Wong, 2000: The Advanced Regional Prediction System (ARPS)—A multiscale nonhydrostatic atmospheric simulation and prediction tool. Part I: Model dynamics and verification. *Meteor. Atmos. Phys.,* **75,** 161–193.

——, and Coauthors, 2001: The Advanced Regional Prediction System (ARPS)—A multi-scale nonhydrostatic atmospheric simulation and prediction tool. Part II: Model physics and applications. *Meteor. Atmos. Phys.,* **76,** 143–166.

——, D.-H. Wang, J.-D. Gao, K. Brewster, and K. K. Droegemeier, 2003: The Advanced Regional Prediction System (ARPS), storm-scale numerical weather prediction and data assimilation. *Meteor. Atmos. Phys.,* **82,** 139–170.

Young, G. S., D. A. R. Kristovich, M. R. Hjelmfelt, and R. C. Foster, 2002: Rolls, streets, waves, and more: A review of quasi-two-dimensional structures in the atmospheric boundary layer. *Bull. Amer. Meteor. Soc.,* **83,** 997–1001.

Ziegler, C. L., and C. E. Hane, 1993: An observational study of the dryline. *Mon. Wea. Rev.,* **121,** 1134–1151.

——, and E. N. Rasmussen, 1998: The initiation of moist convection at the dryline: Forecasting issues from a case study perspective. *Wea. Forecasting,* **13,** 1106–1131.

——, W. J. Martin, R. A. Pielke, and R. L. Walko, 1995: A modeling study of the dryline. *J. Atmos. Sci.,* **52,** 263–285.

——, T. J. Lee, and R. A. Pielke Sr., 1997: Convective initiation at the dryline: A modeling study. *Mon. Wea. Rev.,* **125,** 1001–1026.